Supporting Information

Synergistically Promoting Proton-Coupled Electron Transfer of Oxygen Reduction with Dual Atomic Sites on High-curvature Carbon-onions for High-efficient Zn-Air batteries

Yunxiang Lin[a,b†], Qixin Wang[a,†], Ruyun Zheng[a,†], Bo Geng[a], Yuanyue Bao[b], Anhui Ke[b], Chao Wang[a], Hengjie Liu[c], Xue Liu[a], Lei Shan[a]*, Li Yang[a]* and Li Song[c]*

[a.] Institutes of Physical Science and Information Technology, Leibniz International Joint Research Center of Materials Sciences of Anhui Province, Center of Free Electron Laser & High Magnetic Field, Anhui University, Hefei, 230601, China

[b.] School of Materials Science and Engineering, Key Laboratory of Structure and Functional Regulation of Hybrid Materials, Anhui University, Hefei, 230601, China

[c.] National Synchrotron Radiation Laboratory, University of Science and Technology of China, Hefei, 230029, China

[d.] Email: lshan@ahu.edu.cn *(L. Shan)*; yangli91@mail.ustc.edu.cn *(L. Yang)*; song2012@ustc.edu.cn *(L. Song)*

† These authors contributed equally to this work.

Experimental

Synthesis of Onion-Cr_{SA}

First, 100 mg of CNOs was added to 25 mL of ethanol and sonicated for 30 minutes to ensure uniform dispersion. Next, 3.13 mL of a 0.01 M $CrCl_3$ ethanol solution was slowly added, and the mixture was sonicated again for 30 minutes. The resulting solution was then stirred magnetically at 80 °C to evaporate the remaining ethanol. The obtained solid product was ground into a fine powder and then annealed at 350 °C for 2 h under an ammonia atmosphere with a heating rate of 5 °C min^{-1}, successfully yielding a black Onion-Cr_{SA} substrate.

Synthesis of Onion-$CrFe_{DSA}$

For the Onion-$CrFe_{DSA}$ sample, 100 mg of the prepared Onion-Cr_{SA} substrate was first uniformly dispersed in 25 mL of ethanol to form Solution A. Then, 18 mg of FePc was dispersed in 10 mL of ethanol to form Solution B. Solution B was added to Solution A, and the mixture was ultrasonicated and magnetically stirred for 24 h to ensure thorough mixing. The resulting mixture was then centrifuged several times with ethanol, followed by vacuum drying overnight. The final solid product was ground into a fine powder, resulting in a black Onion-$CrFe_{DSA}$ powder.

Synthesis of Onion-Fe_{SA}

The preparation of Onion-Fe_{SA} is essentially the same as that of Onion-$CrFe_{DSA}$, except that CNOs are used instead of Onion-Cr_{SA}.

Characterizations

The crystal structure of the sample was analyzed using X-ray diffraction (XRD) with an 18 kW advanced X-ray diffractometer employing Cu Kα radiation (λ = 1.54056 Å). Morphological and microstructural observations were made using a JEOL-F200 field emission TEM at an accelerating voltage of 200 kV, and energy-dispersive X-ray spectroscopy (EDS) mapping images were obtained under a scanning TEM mode. The HAADF-STEM images were collected using a Titan Themis Z field emission TEM. Metal content analysis was performed by inductively coupled plasma atomic emission spectroscopy (ICP-AES). The elemental composition was further examined by X-ray photoelectron spectroscopy (XPS) using a Mg Kα monochromatic X-ray source. The physical adsorption of N_2 was analyzed using a BSD-PS1/2/4 surface area and pore size analyzer at 77.3 K. Raman spectroscopy was conducted with a Horiba Odyssey Raman microscope. X-ray absorption fine structure (XAFS) spectra were recorded at beamline BL14W1 of the Shanghai Synchrotron Radiation Facility (SSRF). Synchrotron radiation Fourier transform infrared spectroscopy was performed at the National Synchrotron Radiation Laboratory (NSRL) on beamline BL01B. The XAFS data was analyzed by ATHENA and ARTEMIS software. The background signals of absorption curves were firstly deducted and the then normalized to 1. The FT-EXAFS curves, which reflect the local configuration in R space, were obtained by Fourier transformed χ(k) function using Hanning window in the range of 2.8 to 11.3 $Å^{-1}$ (dk=1.0 $Å^{-1}$). The FT-EXAFS data was fitted by ARTEMIS software: Firstly, the amplitude reduction factors (S_0^2) was obtained by fitting the standard sample with fixed coordination number; Secondly, the local coordination information of Fe and Cr by fitting the FT-

EXAFS spectra using obtained amplitude reduction factors and different structure parameter until the fitting data is highly consistent with experimental data.

Electrochemical measurements

Electrochemical measurements were performed using a standard three-electrode system on a CHI760E electrochemical workstation (Shanghai Chenhua Co., Ltd.). A rotating disk electrode (RDE) with a diameter of 5 mm was used as the working electrode, with a Pt mesh (1 cm^2, Tianjin Aida Co., Ltd.) as the counter electrode and a saturated Ag/AgCl electrode (saturated KCl, Tianjin Aida Co., Ltd.) as the reference electrode. 0.1 M KOH was used as the electrolyte. The pH of the electrolyte (pH = 12.98 ± 0.02) was measured using a pH meter, which was calibrated with pH buffer solutions (pH = 4.00, pH = 6.86, pH = 9.18). All tests were conducted at room temperature. For the ORR test, 5 mg of the electrocatalyst was mixed with 700 μL of isopropanol, 300 μL of deionized water, and 50 μL of a 5 wt% Nafion solution to form a 1.05 mL solution. This mixture was sonicated for 1 h to prepare a homogeneous catalyst ink. Then, 10 μL of the catalyst ink was applied to the GCE (with a loading of 0.256 mg cm^{-2}) and dried at room temperature. Prior to electrochemical measurements, the electrolyte was bubbled with N_2/O_2 for 30 minutes and continuously bubbled throughout the ORR test to ensure the electrolyte was saturated with N_2/O_2. The cyclic voltammetry (CV) scan rate was 100 mV s^{-1}. Linear sweep voltammetry (LSV) was performed in the range of 0.2-1.1 V (vs RHE) with a scan rate of 5 mV s^{-1} and a rotation speed of 225 rpm to 2025 rpm. All data were collected without iR-compensation. All measured potentials were converted to the reversible hydrogen electrode (RHE) potential using the Nernst equation. The double-layer capacitance (C_{dl}) was measured using CV measurements within the non-Faradaic voltage range of 1.00 V to 1.20 V (vs RHE) and its variation was recorded over the scan rates of 20 mV s^{-1} to 120 mV s^{-1}. The value of $\Delta_{j/2}$ at 1.10 V (vs RHE) was plotted as a function of the scan rate, and the slope was fitted to represent the C_{dl} value. Electrochemical impedance spectroscopy (EIS) measurements were conducted over a frequency range of 0.01 Hz to 100 kHz, with an alternating current amplitude of 5 mV.

The kinetic current density (J_K) was calculated based on the Koutecky-Levich equation:

$$\frac{1}{J} = \frac{1}{J_K} + \frac{1}{J_L} = \frac{1}{J_K} + \frac{1}{B\omega^{1/2}}$$

$$B = 0.62nFC_0D_0^{2/3}\nu^{-1/6}$$

Where J represents the measured current density, while J_K and J_L refer to the kinetic current density and the limiting diffusion current density, respectively. ω is the angular velocity of the GCE, n is the number of electrons transferred, F is the Faraday constant (96,485 C mol^{-1}), C_0 is the bulk concentration of O_2 (1.2×10^{-6} mol cm^{-3}), D_0 is the diffusion coefficient of O_2 in 0.1 M KOH solution (1.9×10^{-5} cm^2 s^{-1}), and ν is the kinematic viscosity of the electrolyte (0.01 cm^2 s^{-1}). The number of electron transfers at different potentials was calculated using the Koutecky-Levich equation at various rotation speeds (225, 400, 625, 900, 1225, 1600, and 2025 rpm). The rotation speed was converted into angular velocity (ω).

The stability of the catalyst was evaluated using chronoamperometry at a constant potential of 0.5 V (vs RHE) in 0.1 M KOH, with the GCE rotating at 1600 rpm. The catalyst's resistance to methanol poisoning was also assessed using chronoamperometry. During the test, 3 M methanol was added, and the change in the i-t curve before and after methanol addition was used to evaluate the catalyst's ability to resist methanol poisoning. The catalyst's resistance to SCN^- poisoning was assessed by comparing the LSV curves before and after the addition of 10 mM KSCN to the electrolyte.

The number of electron transfers and the hydrogen peroxide yield were determined using a rotating ring-disk electrode (RRDE). The measurements were conducted using LSV curves in the range of 0.2 to 1.1 V (vs RHE) with a scan rate of 5 mV s^{-1} and a rotation speed of 1600 rpm. The potential of the ring electrode was set at 1.2 V (vs RHE). The number of electron transfers (n) and the hydrogen peroxide yield (H_2O_2%) were calculated using the following two equations:

$$n = 4 \times \frac{I_d}{I_d + I_r/N}$$

$$H_2O_2\% = 200 \times \frac{I_r/N}{I_d + I_r/N}$$

Where I_d and I_r represent the disk current and ring current, respectively. N is the hydrogen peroxide collection factor at the ring (N = 0.37).

The intrinsic activity of the sample was evaluated using mass activity (MA) and turnover frequency (TOF). Considering the atomic dispersion of iron single atoms and the porous nature of the prepared catalyst, we assume that all Fe sites are accessible in the calculation. The MA of the catalyst is calculated using the following equation:

$$MA = \frac{J_K \times A}{M}$$

Where J_K is the kinetic current density calculated using the Koutecky-Levich (K-L) equation, A is the surface area of the working electrode (0.196 cm^2), and M is the metal loading mass of the electrocatalyst on the electrode surface. The metal content was determined using ICP-AES.

The TOF of the catalyst is calculated using the following equation:

$$TOF = \frac{J_K \times A}{4NF}$$

Where J_K is the kinetic current density calculated using the Koutecky-Levich (K-L) equation, A is the surface area of the working electrode (0.196 cm^2), N is the number of Fe atoms determined by ICP-AES, and F is the Faraday constant. The value of N for 20 wt% Pt/C is determined using the following equation:

$$N = \omega_{Pt} \times C_{cat} \times D/M_{Pt}$$

Where ω_{Pt} represents the Pt concentration of Pt/C, C_{cat} is the mass loading of Pt/C catalyst on the GCE, D is the dispersion (26%), and M_{Pt} is the molar mass of Pt.

Zn-Air battery tests

The performance of the zinc-air battery was evaluated using an electrochemical workstation (CHI 760E) and a battery testing system (LANHE CT3002A). The battery was assembled with an anode (0.3 mm polished Zinc plate), an air cathode (a composite cathode consisting of a carbon paper/hydrophobic layer/nickel foam structure, with the

electrocatalyst loading of 1 mg cm^{-2}), and an electrolyte (6 M KOH containing 0.2 M zinc acetate).

For flexible ZAB measurement, open-circuit voltage was measured using a multimeter and a CHI 760E electrochemical workstation. LSV curves (discharge) were recorded using the CHI 760E electrochemical workstation. The specific capacity of the battery was tested using a LANHE system through constant current discharge (10 mA cm^{-2}), with the curve normalized by the consumed zinc mass. Long-term discharge stability tests were conducted under the same conditions as the specific capacity measurements. The rate performance was evaluated by constant current discharge at current densities of 5, 10, 20, and 50 mA cm^{-2}, followed by a return to 5 mA cm^{-2}, with each discharge step lasting one hour. The durability of the battery was assessed through constant current discharge/charge cycling tests, using the catalyst (Onion-$CrFe_{DSA}$ or 20 wt% Pt/C) dispersed as ink with commercial RuO_2 in a 1:1 mass ratio. The total catalyst loading on the composite cathode was 2 mg cm^{-2}. Discharge/charge cycling measurements were conducted at a current density of 10 mA cm^{-2} using the LANHE system at room temperature, with each cycle lasting 20 minutes (10 minutes for discharge followed by 10 minutes for charge).

***Operando* measurements**

Operando ATR-SEIRAS measurements were performed in attenuated total reflection mode using a conventional three-electrode system at the NSRL BL01B beamline. A semi-cylindrical silicon prism with a 50 nm gold film coating was used for reflection. The catalyst was evenly dispersed in a 1 mL ethanol solution, and the catalyst ink was applied to the gold film and dried at room temperature to prepare the working electrode. A Pt mesh (1 cm^2) and Ag/AgCl electrode served as the counter and reference electrodes, respectively, with 0.1 M KOH as the electrolyte. Spectra were collected using a Bruker Vertex 80 V spectrometer equipped with a liquid nitrogen-cooled mercury cadmium telluride (LN-MCT) detector, averaging 64 scans at a resolution of 4 cm^{-1}. Background spectra were recorded at open-circuit voltage, and subsequent spectra were acquired under incremental potential steps.

Operando Raman spectroscopy analysis was conducted using a Horiba Odyssey Raman microscope. The catalyst was first loaded onto carbon paper and then assembled onto the electrochemical cell. A 532 nm wavelength laser was used with a 50x long-focus objective. Spectral shifts were calibrated using a Si wafer at 520.7 cm^{-1}. Electrochemical Raman spectra were collected using a chronoamperometry method at different reaction potentials.

Operando XAFS measurement was conducted in a traditional three-electrode electrochemical cell conducted by Si (111) mode at BL14W1 of SSRF (Supplementary Fig. S53a), in which the absorption edge of measured elements was corrected by foil sample. The catalyst was uniformly dispersed in 1 mL ethanol solution and then dropped onto the carbon paper to prepare a working electrode. The Pt mesh (1 cm^2) and Hg/HgO electrode served as the counter electrode and reference electrode, while the oxygen saturated 0.1 M KOH solution was served as the electrolyte. The XAFS data were collected at different reaction potentials by chronopotentiometry after CV cycling

for 20 min. The obtained data were analyzed by ARTEMIS software containing the FEFF code.

Theoretical calculations

All calculations in this study were performed using density-functional theory (DFT) as implemented in the Vienna Ab initio Simulation Package (VASP). The generalized gradient approximation (GGA) with the Perdew–Burke–Ernzernhof (PBE) exchange-correlation functional was employed for geometric optimization and electronic structure analysis. The projector augmented wave (PAW) method was utilized to describe the interactions between core and valence electrons. A kinetic energy cutoff of 450 eV was applied, and the Brillouin zone was sampled using a Monkhorst-Pack k-mesh of 1 × 1 × 1, appropriate for isolated systems. The energy convergence criterion for the electronic self-consistent field iterations was set at 10^{-5} eV, the maximum residual force was limited to 0.02 eV·Å^{-1} to ensure reliable structural and energetic calculations. The transition states (TS) for water dissociation were defined using the climbing image nudged elastic band (CI-NEB) method, which is widely adopted to investigate reaction pathways on various catalytic surfaces. To eliminate interactions between periodic images, a vacuum layer of 15 Å was introduced along the z-direction. The Gibbs free energy change associated with the reaction was evaluated using the following equation:

$$\Delta G = \Delta E + \Delta ZPE - \mathrm{T}\Delta S$$

where ΔE is the reaction energy change obtained from the DFT calculations, ΔZPE denotes the change of zero-point energy, and ΔS is the entropy change, T is the temperature, set to 298.15 K.

The adsorption energies between H_2O on catalyst surfaces were calculated using the following formula:

$$E_{ads} = E_{substrate/H2O} - (E_{substrate} + E_{H2O})$$

Here, $E_{substrate/H2O}$ denotes the DFT-computed energy of the catalyst surface(substrate) adsorbed with H_2O molecule, while $E_{substrate}$ and E_{H2O} correspond to the energies of the pristine substrate and isolated H_2O molecule, respectively. A more negative E_{ads} value presents a stronger binding interaction between the adsorbate and the substrate surface, indicating a more thermodynamically favorable adsorption configuration.

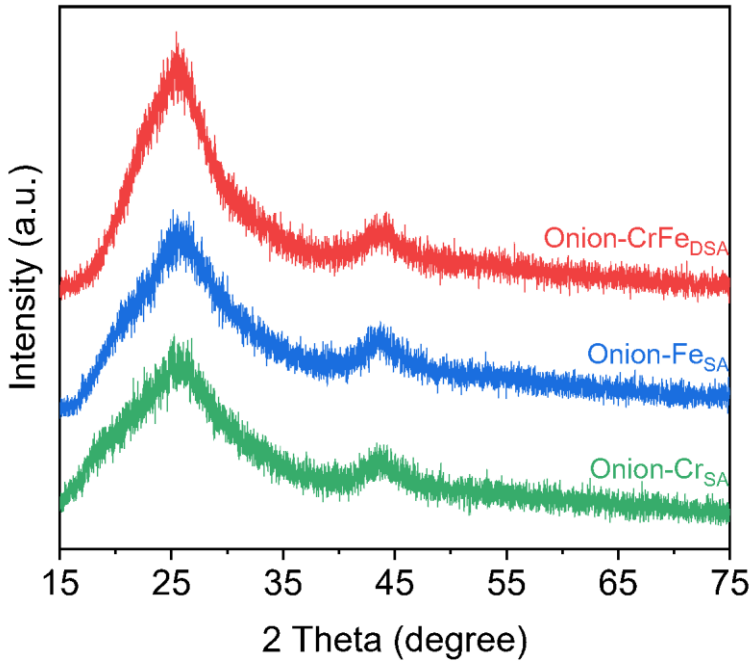

Figure S1. XRD patterns of the as-prepared Onion-CrFe$_{DSA}$ and counterparts.

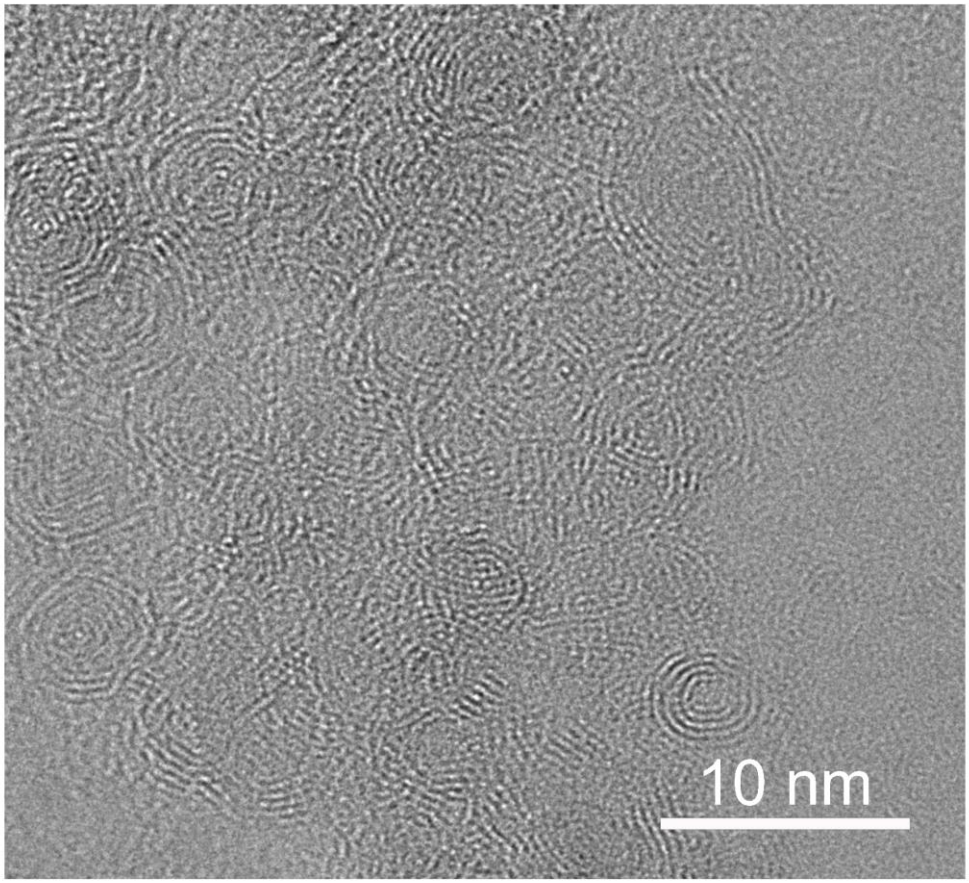

Figure S2. HRTEM images of Onion-Cr_{SA}.

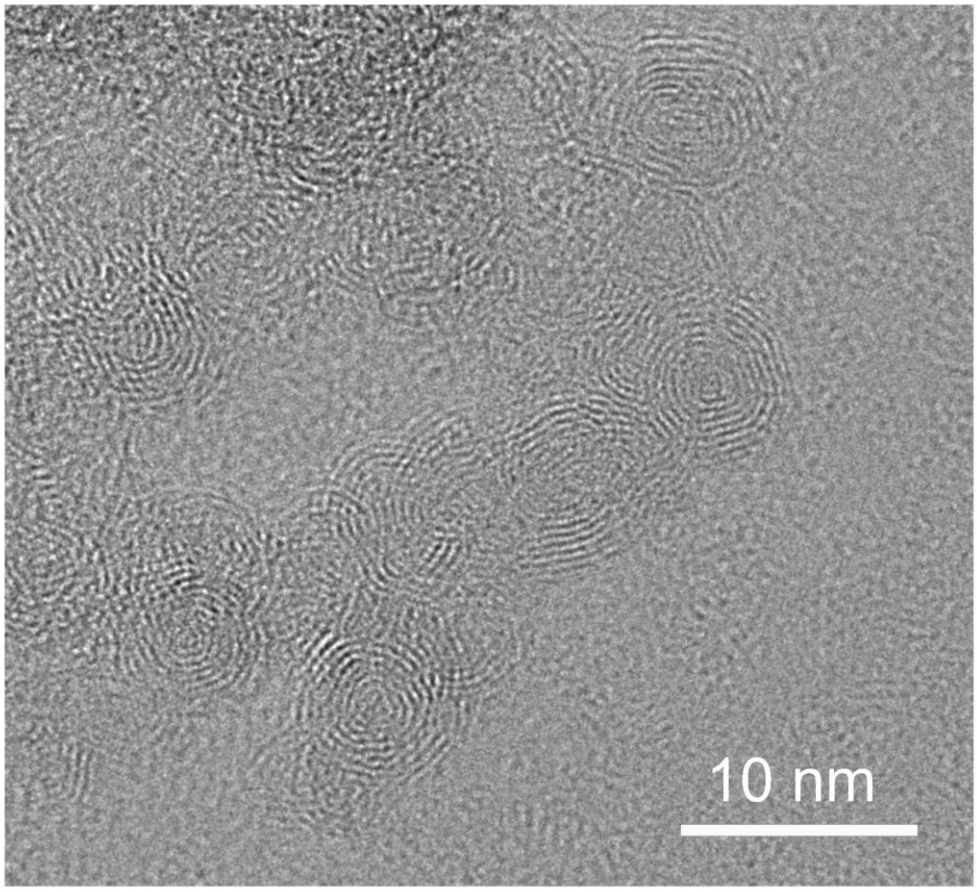

Figure S3. HRTEM images of Onion-Fe_{SA}.

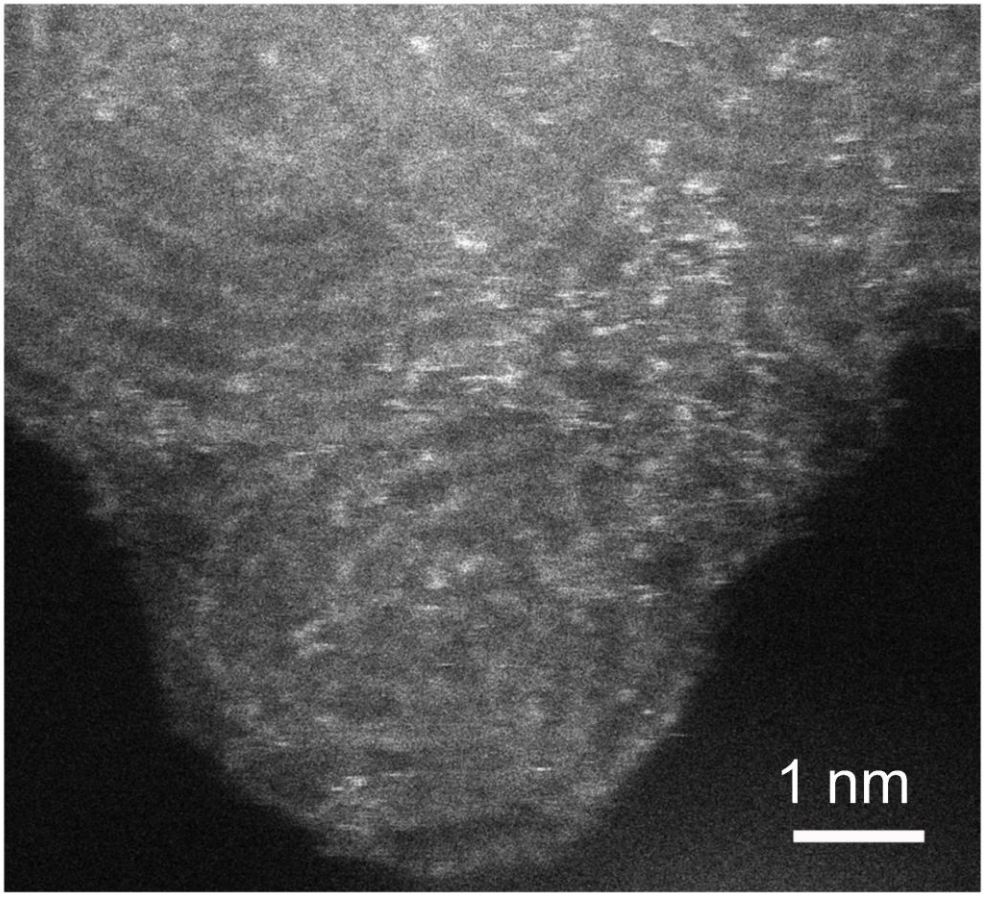

Figure S4. HAADF-STEM images of Onion-Cr_{SA}.

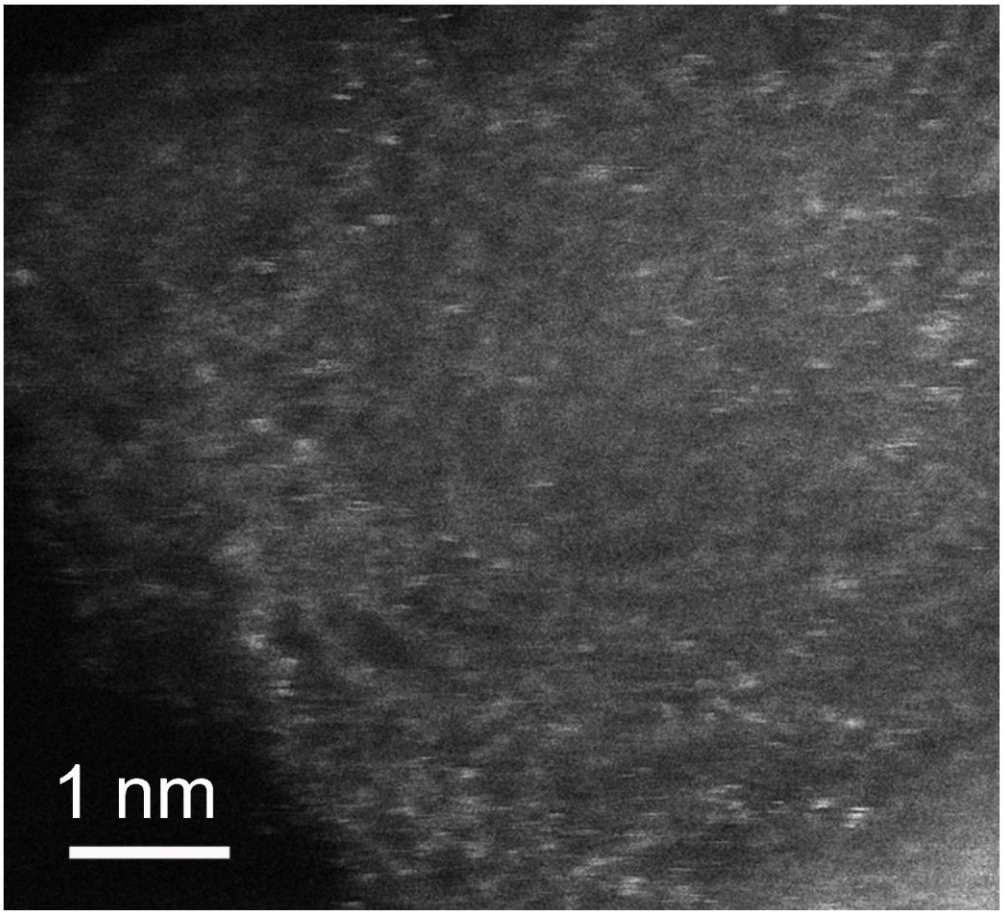

Figure S5. HAADF-STEM images of Onion-Fe_{SA}.

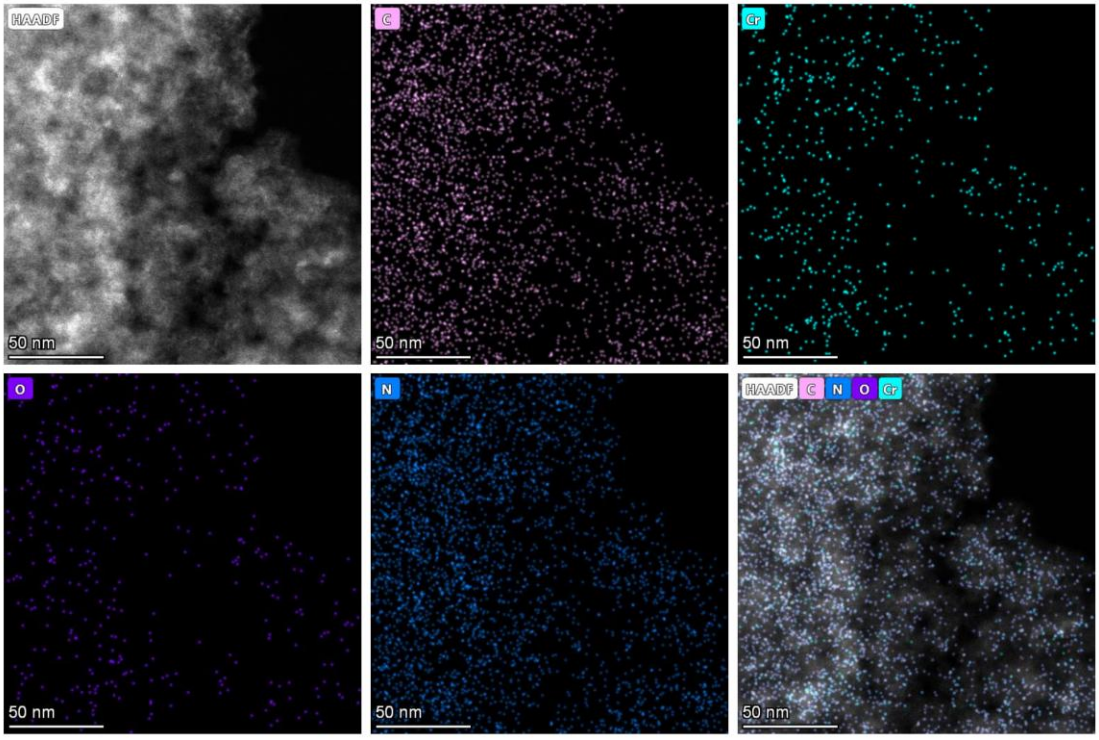

Figure S6. EDS-mapping of the Onion-Cr_{SA}.

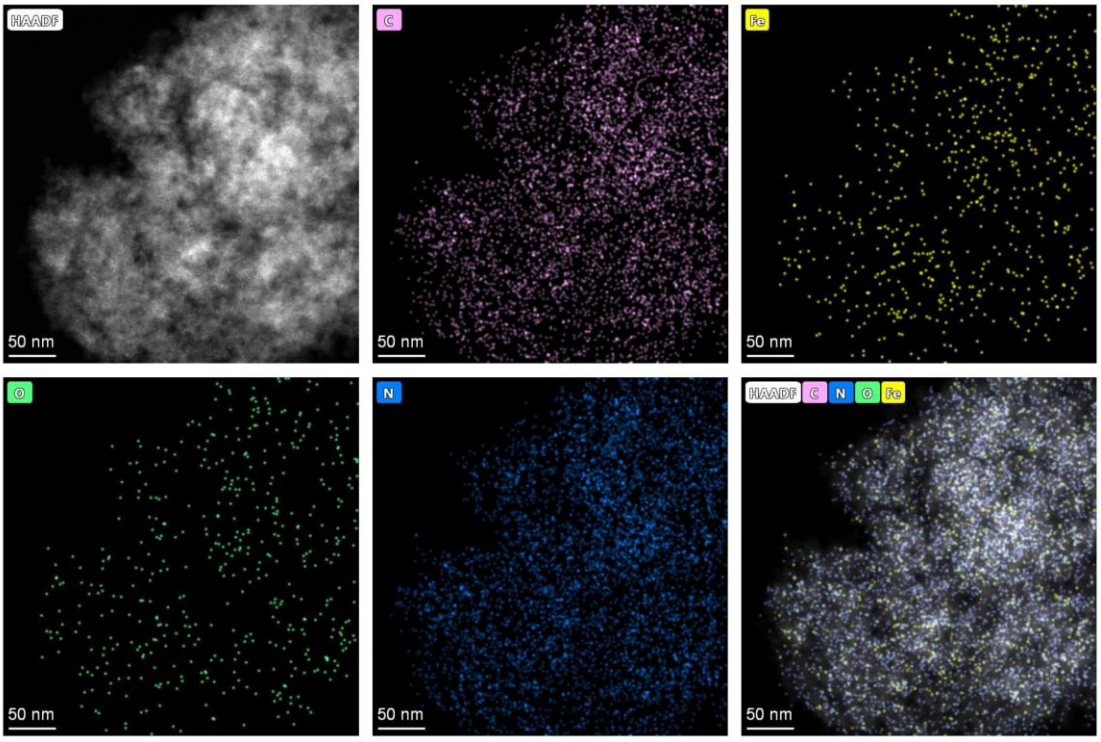

Figure S7. EDS-mapping of the Onion-Fe_{SA}.

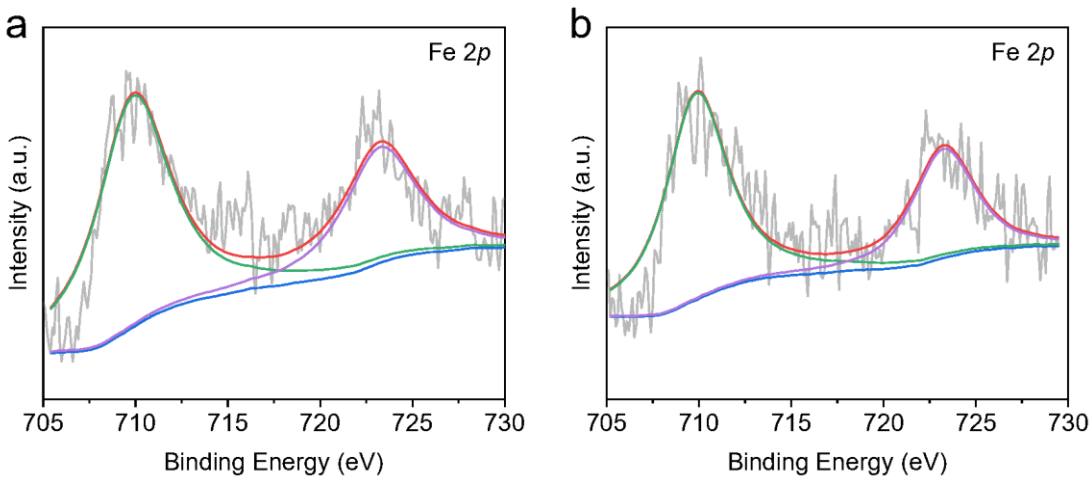

Figure S8. Fe *2p* XPS spectra of the (a) Onion-CrFe$_{DSA}$ and (b) Onion-Fe$_{SA}$.

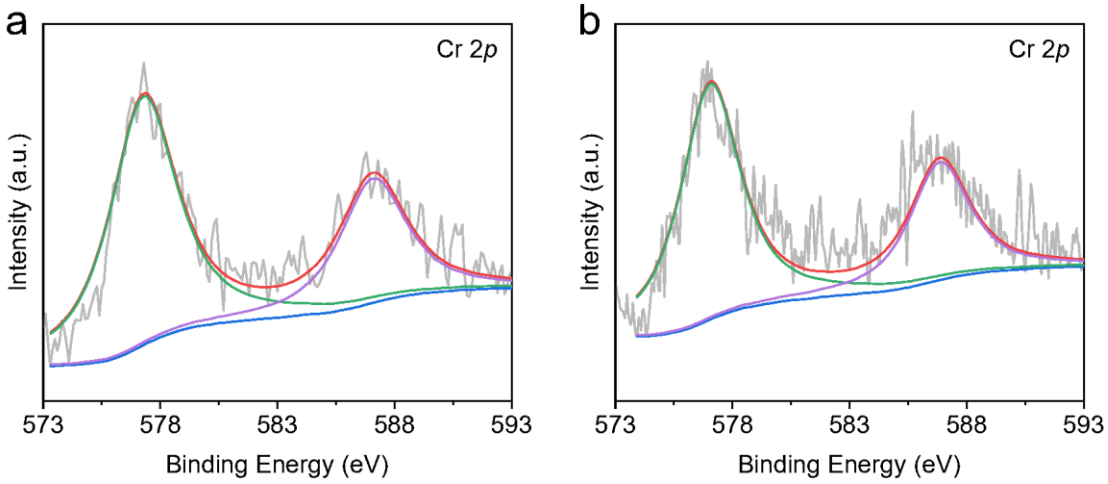

Figure S9. Cr *2p* XPS spectra of the (a) Onion-CrFe$_{DSA}$ and (b) Onion-Cr$_{SA}$.

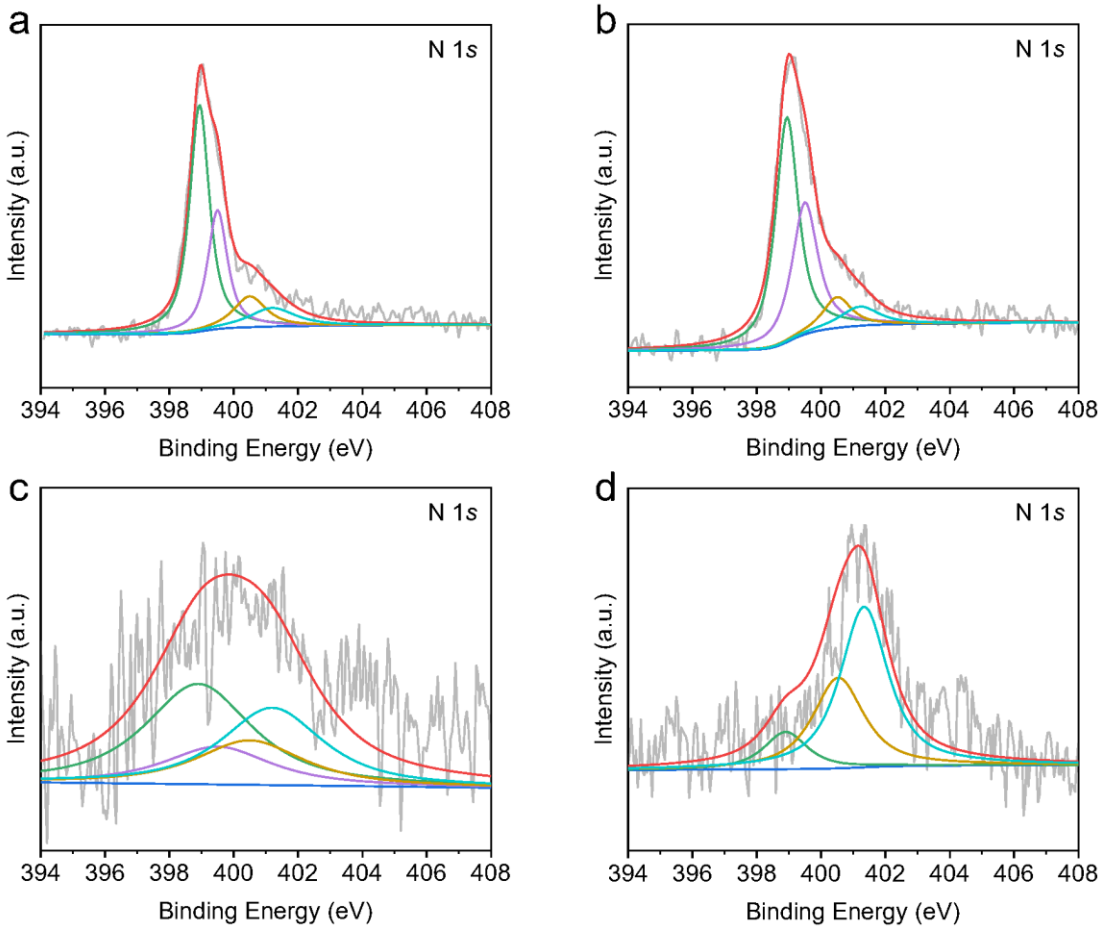

Figure S10. N *1s* XPS spectra of the (a) Onion-CrFe$_{DSA}$, (b) Onion-Fe$_{SA}$, (c) Onion-Cr$_{SA}$, and (d) Onion.Note:

The XPS spectra of N *1s* for Onion-CrFe$_{DSA}$ and Onion-Fe$_{SA}$ exhibit clear peak shapes and high signal intensities, mainly because FePc contains nitrogen. When FePc is added, nitrogen is also introduced into the system, resulting in high signal intensities in the spectra. In contrast, Onion and Onion-Cr$_{SA}$ do not have FePc added; their nitrogen sources come from the commercial carbon nano-onions themselves. These nitrogen sources may be trace nitrogen-containing impurities introduced during the synthesis process, with extremely low content, leading to poor signal-to-noise ratios and weak signals.

The significant difference in N *1s* signals provides strong evidence for the successful introduction of FePc. The weak background signals of the samples without FePc reflect the real background of commercial carbon-based materials; meanwhile, the strong and regular nitrogen signals that appear after FePc addition clearly indicate the successful loading of exogenous FePc molecules.

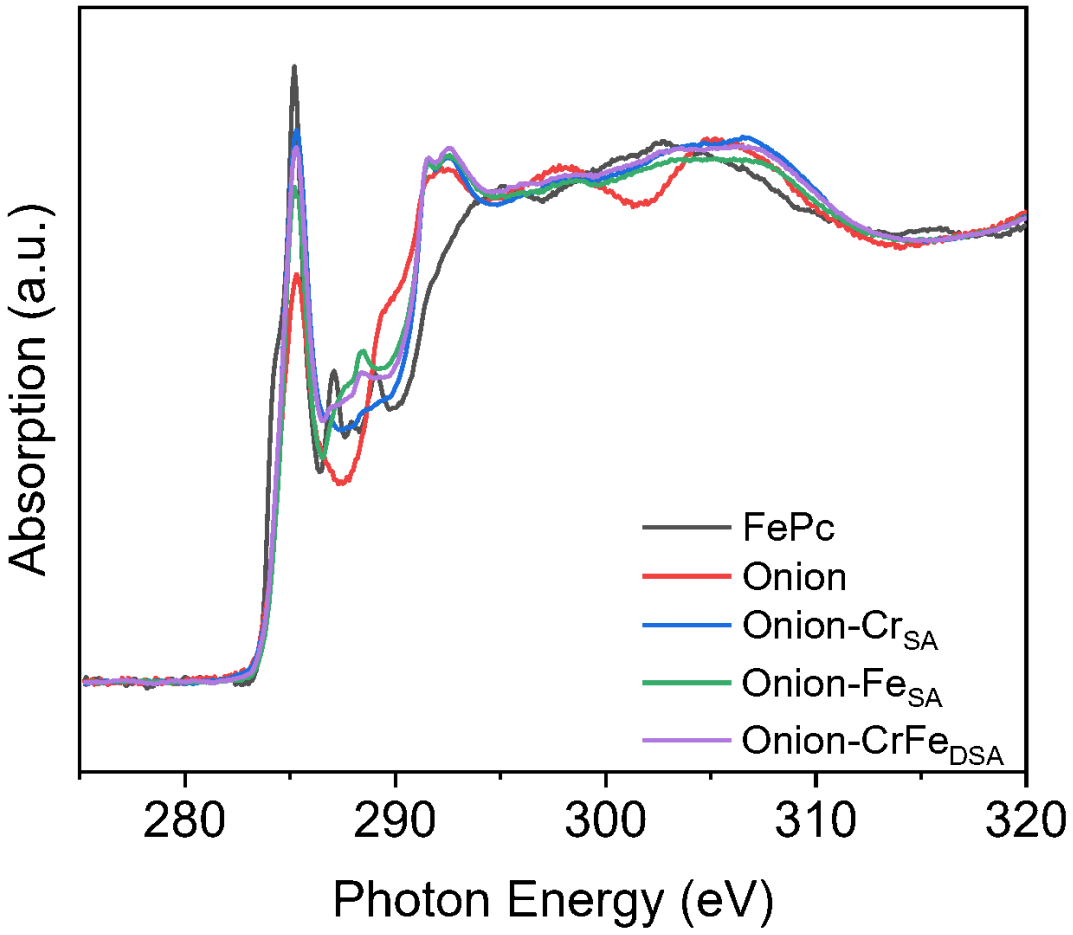

Figure S11. C *K*-edge XANES spectra of the series samples.

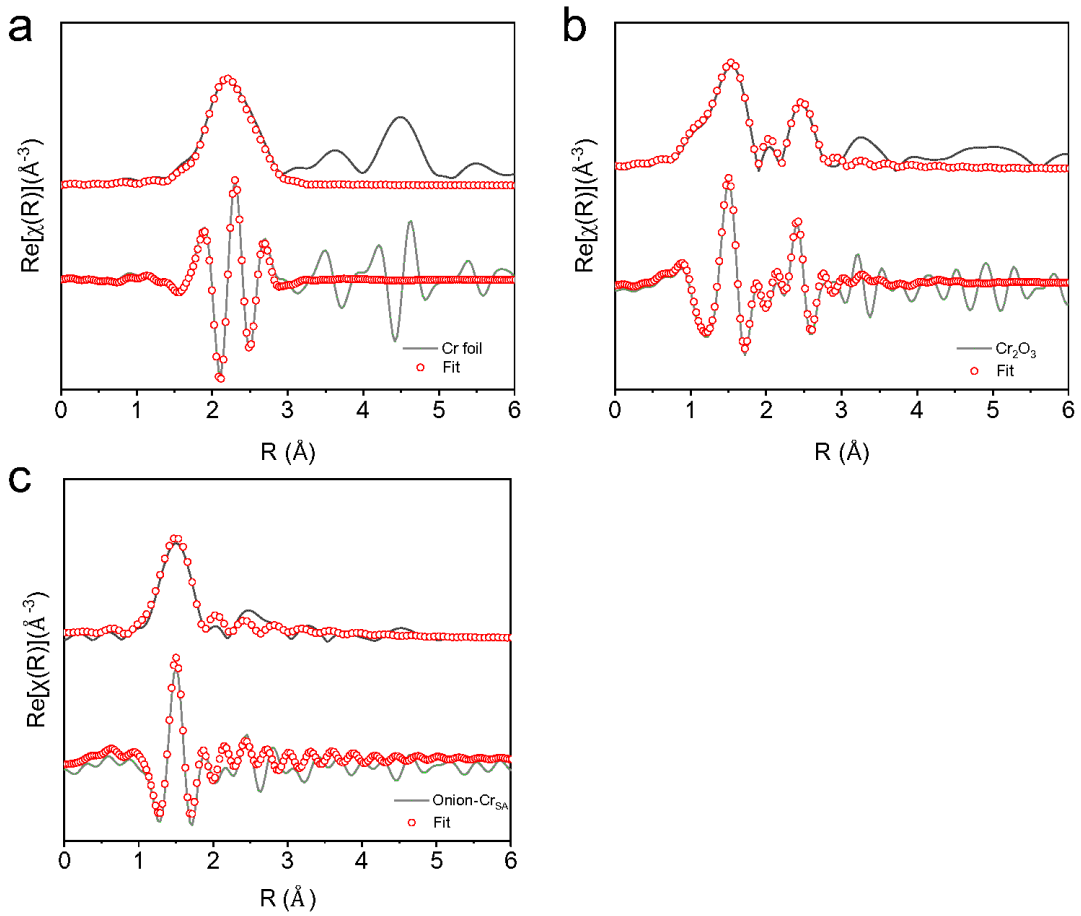

Figure S12. EXAFS fitting curves displayed in R space for (a) Cr foil, (b) Cr_2O_3, (c) Onion-Cr_{SA}.

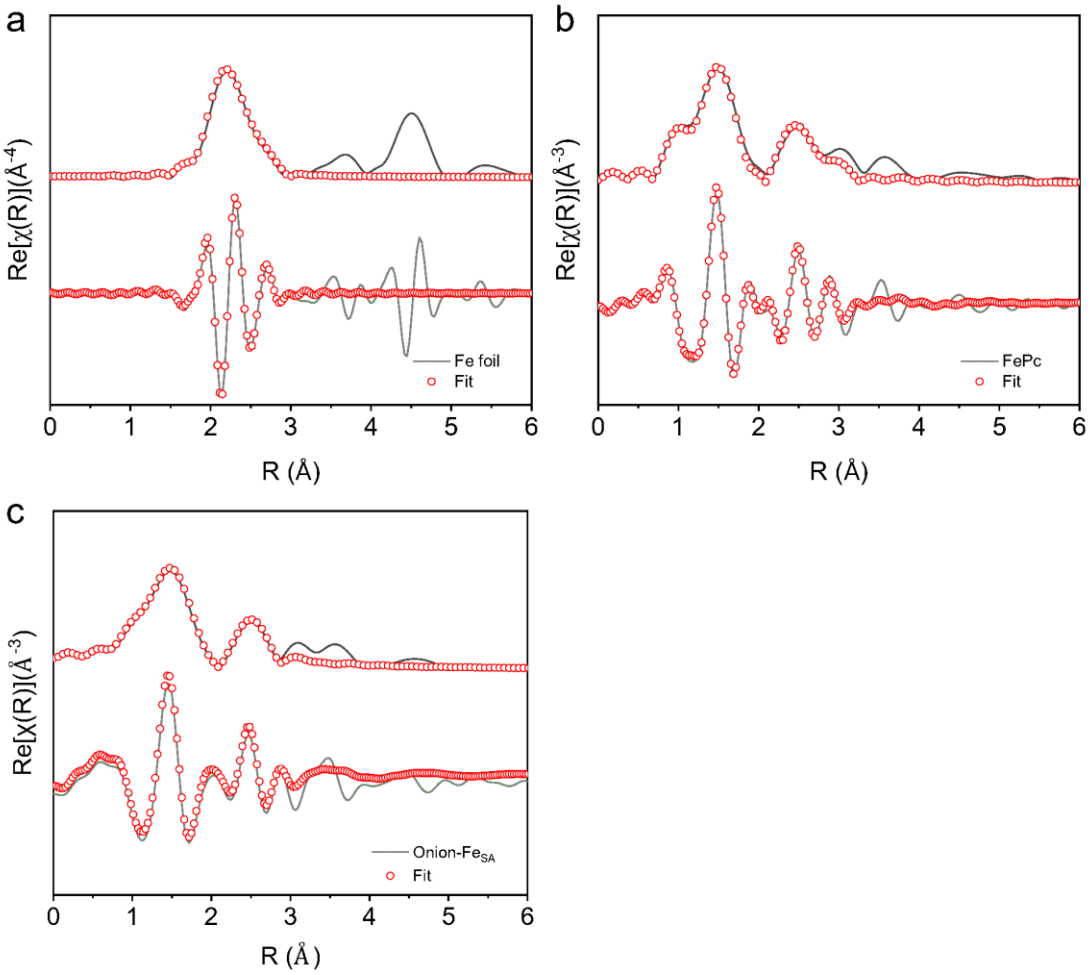

Figure S13. EXAFS fitting curves displayed in R space for (a) Fe foil, (b) FePc, (c) Onion-Fe_{SA}.

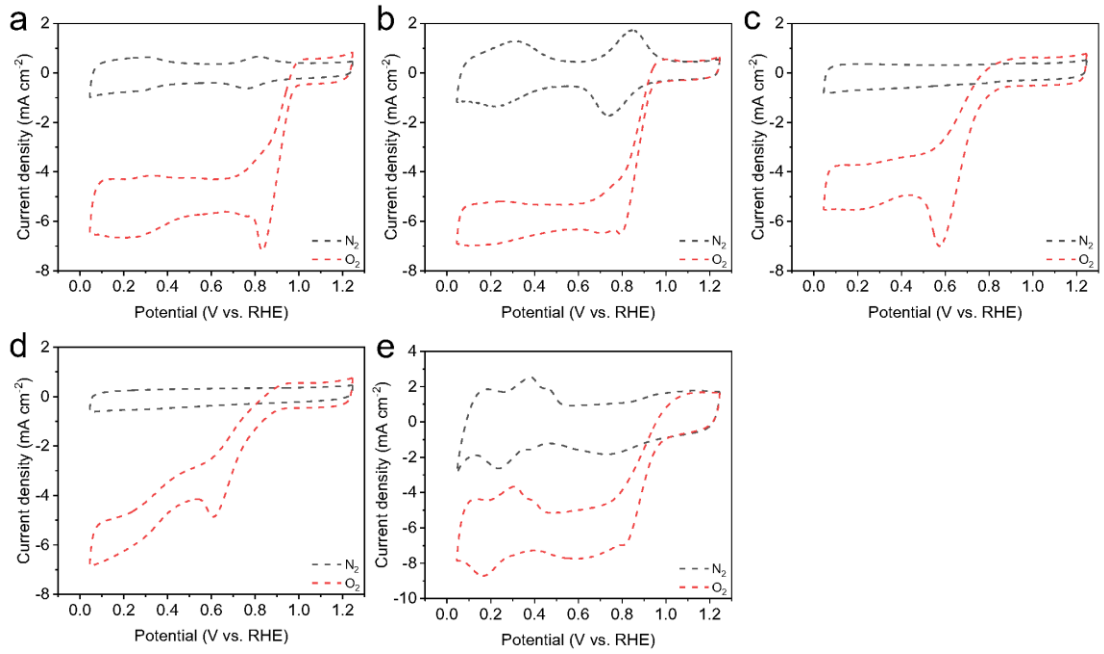

Figure S14. CV curves under N_2 and O_2-saturated electrolyte for (a) Onion-$CrFe_{DSA}$, (b) Onion-Fe_{SA}, (c) Onion-Cr_{SA}, (d) Onion, and (e) 20% Pt/C.

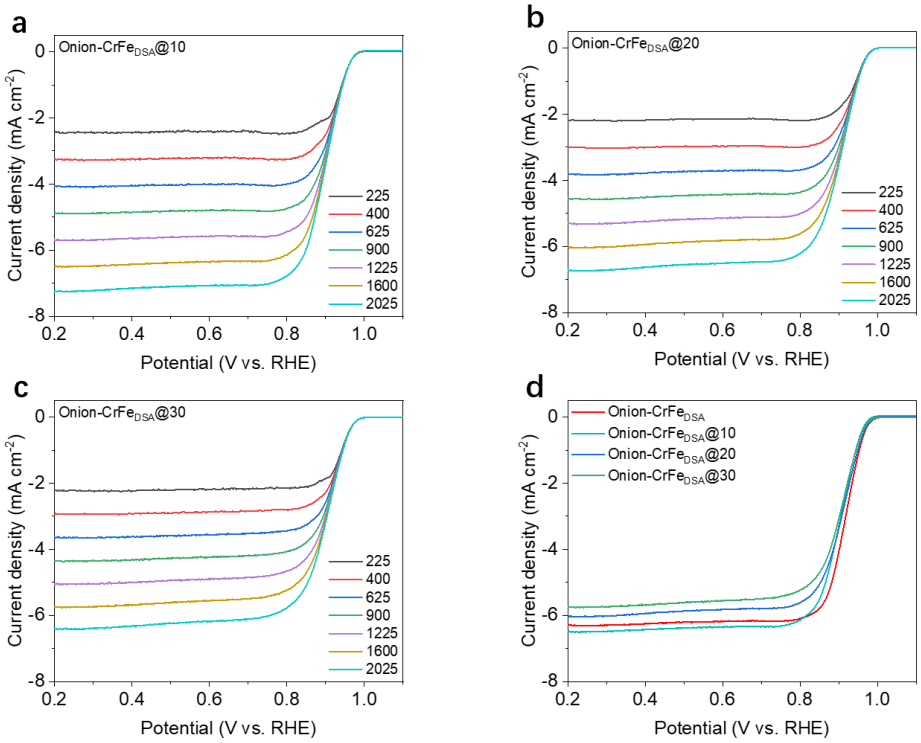

Figure S15. LSV curves of Onion-CrFe$_{DSA}$, Onion-CrFe$_{DSA}$@10, Onion-CrFe$_{DSA}$@20 and Onion-CrFe$_{DSA}$@30 in 0.1 M KOH electrolyte at 1600 rpm.

Note: A series of catalysts with varying Fe loadings by systematically adjusting the amount of FePc molecule (10 mg, 20 mg, and 30 mg) while keeping the Cr loading fixed (using the pre-synthesized Onion-Cr$_{SA}$ support). The Onion-CrFe$_{DSA}$ show the highest $E_{1/2}$ of 0.916 V, which is higher than that of Onion-CrFe$_{DSA}$@20 ($E_{1/2}$ = 0.908 V), Onion-CrFe$_{DSA}$@30 ($E_{1/2}$ = 0.905 V), and Onion-CrFe$_{DSA}$@10 ($E_{1/2}$ = 0.901 V). This indicates the existence of an optimal Fe loading (corresponding to an optimal distribution of atomic spacings), as both excessively high and low loadings lead to decreased activity, indirectly confirming that the Cr-Fe atomic distance significantly influences the synergistic effect.

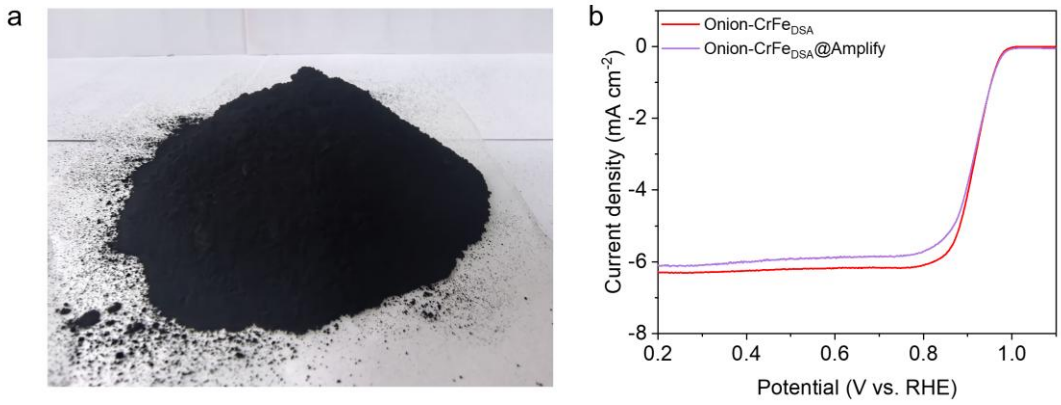

Figure S16. (a) The amplified gram-scale synthesis of the Onion-CrFe$_{DSA}$ and (b) the correspond LSV curve of ORR at 1600 rpm.

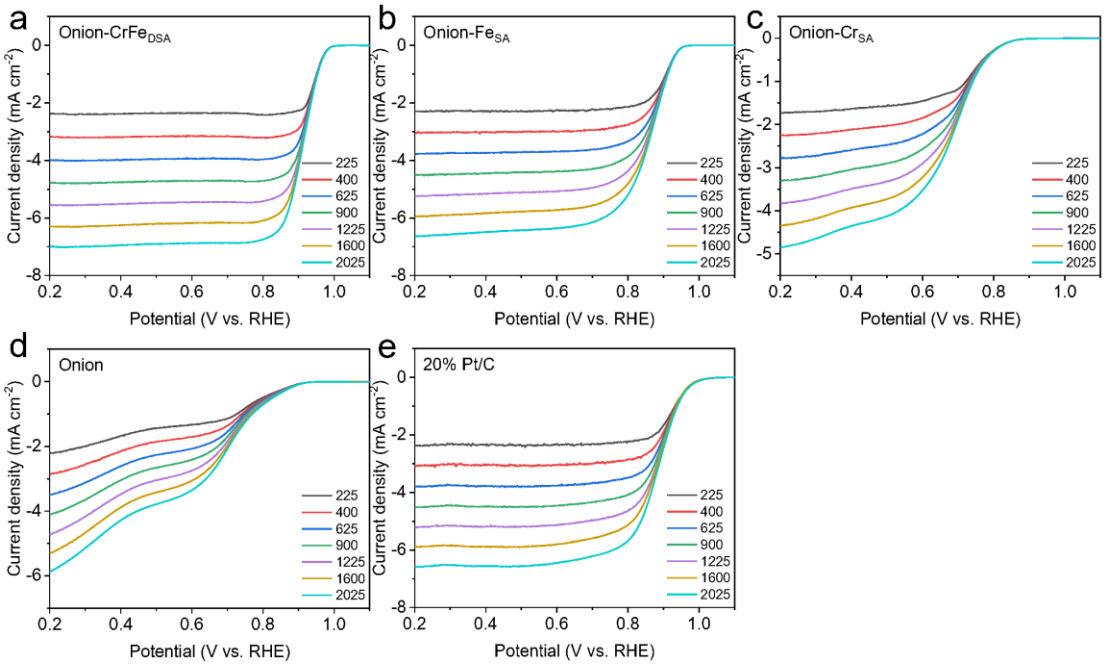

Figure S17. LSV curves under different rotating speed for the as-prepared samples.

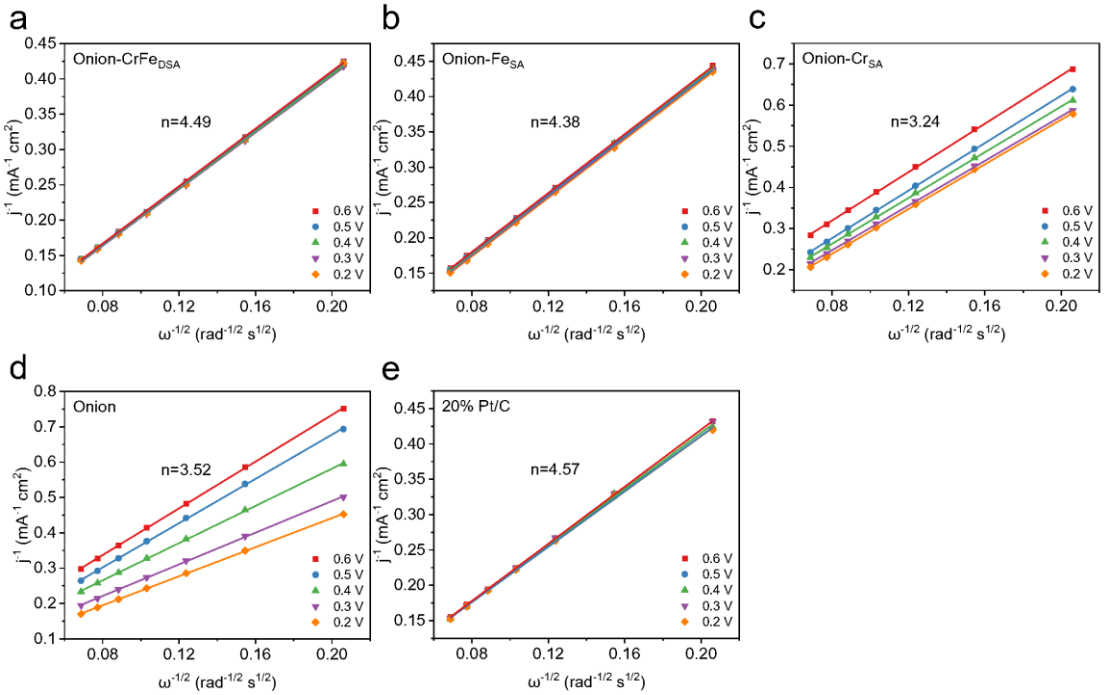

Figure S18. K-L plots of the as-prepared samples under different potentials.

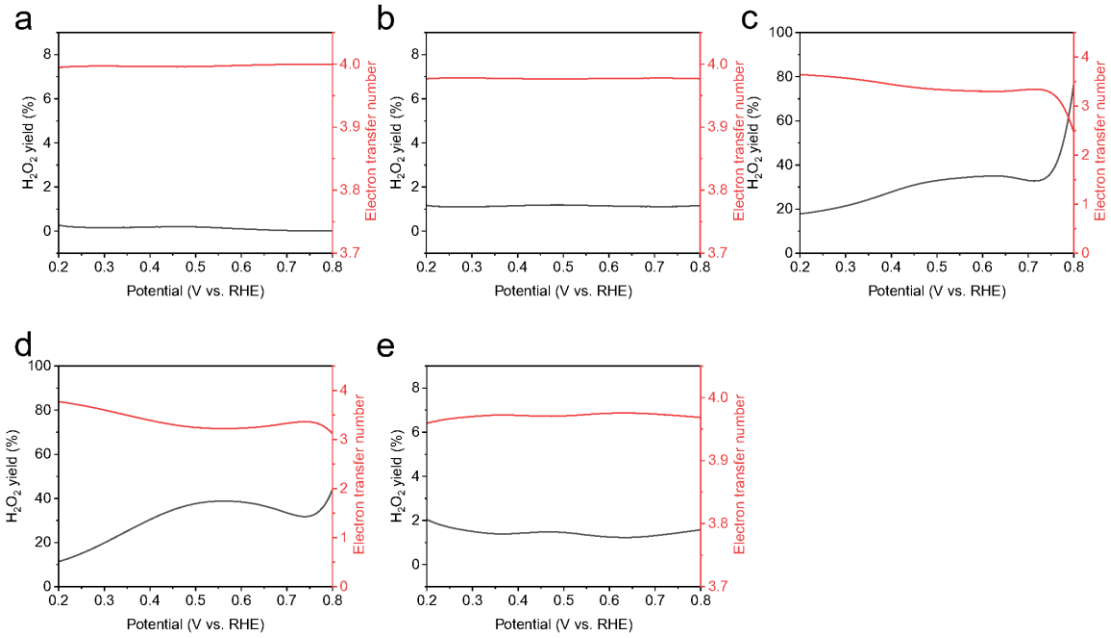

Figure S19. The electron transfer number and H_2O_2 yield obtained from RRDE test for (a) Onion-$CrFe_{DSA}$, (b) Onion-Fe_{SA}, (c) Onion-Cr_{SA}, (d) Onion, and (e) 20% Pt/C.

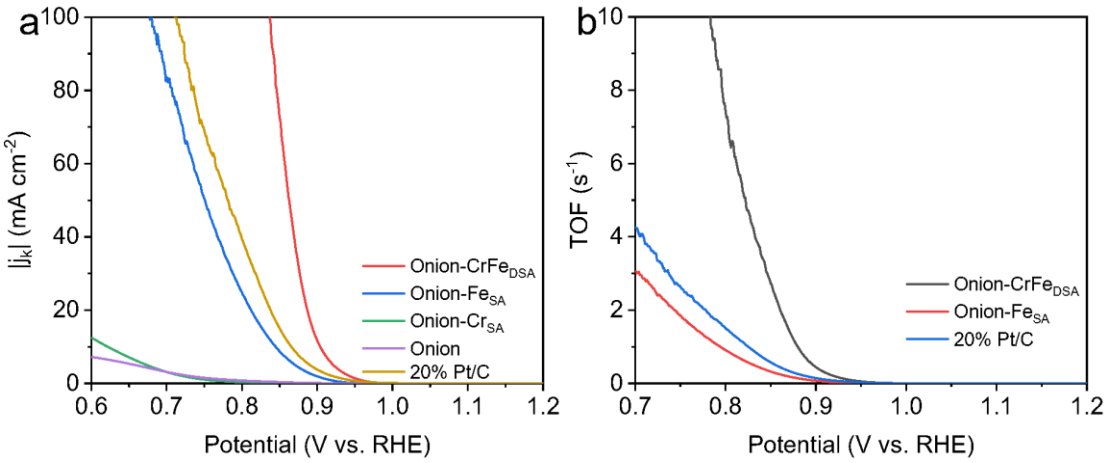

Figure S20. (a) $|J_k|$ and (b) TOF of the series samples.

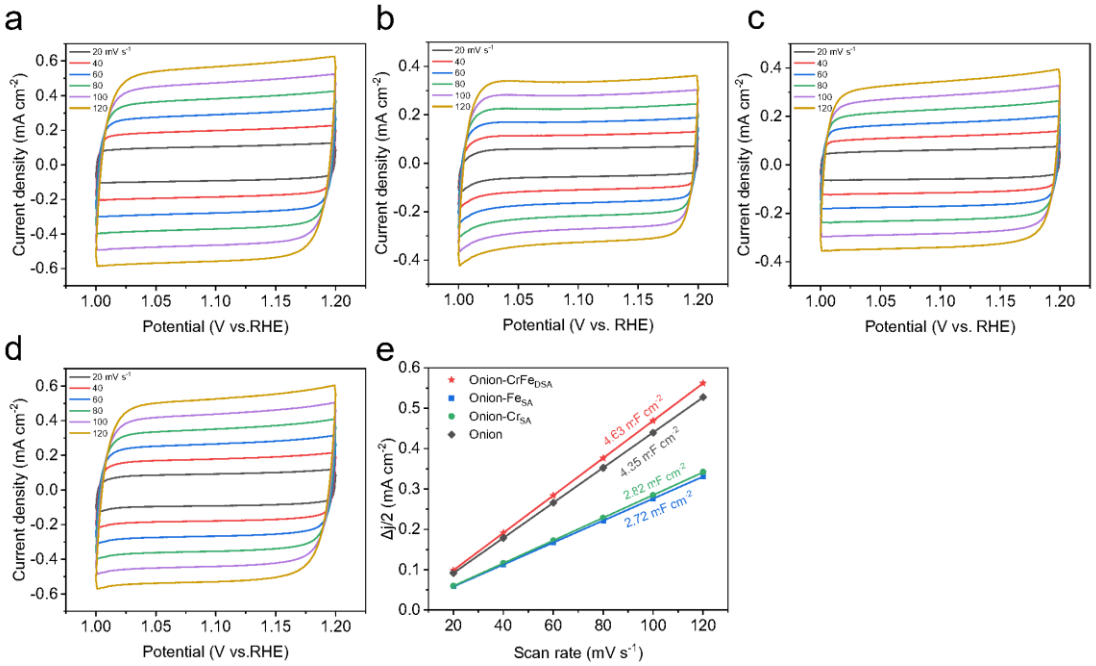

Figure S21. CV curves at non-Faradaic region in 0.1 M KOH with various scan rates of (a) Onion-$CrFe_{DSA}$, (b) Onion-Fe_{SA}, (c) Onion-Cr_{SA}, (d) Onion, (e) and the corresponding C_{dl}.

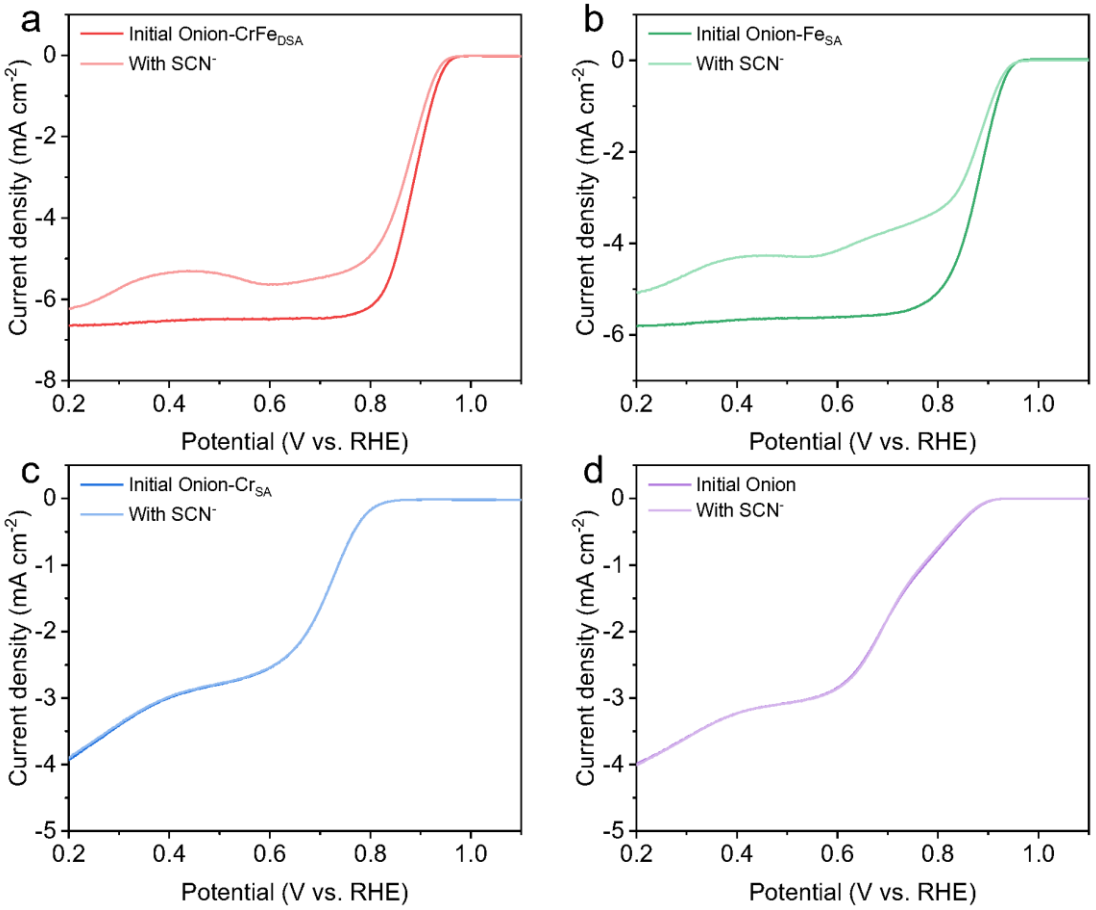

Figure S22. LSV of (a) Onion-$CrFe_{DSA}$, (b) Onion-Fe_{SA}, (c) Onion-Cr_{SA}, and (d) Onion with and without 10 mM SCN^{-1} in O_2-saturated 0.1 M KOH.

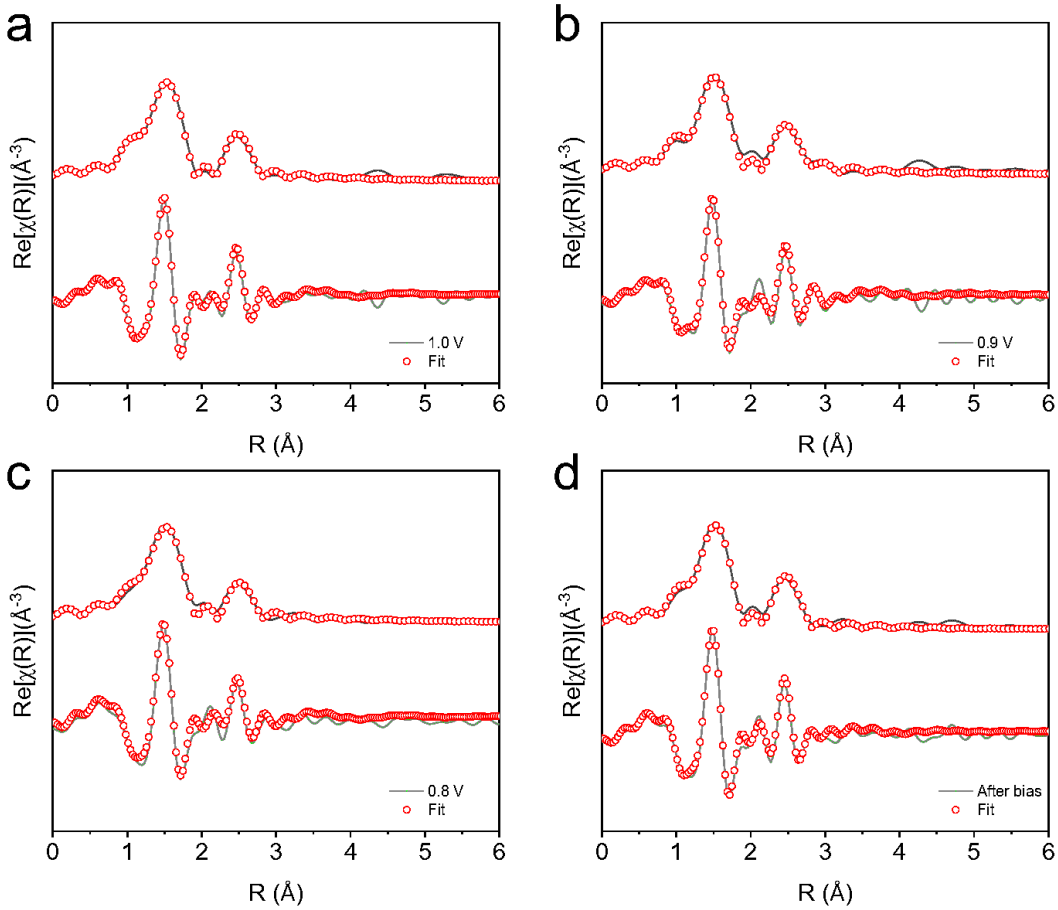

Figure S23. EXAFS fitting results of the Cr *K*-edge spectra for Onion-CrFe$_{DSA}$ at different operate potentials: (a) 1.0 V, (b) 0.9 V, (c) 0.8 V, and (d) after bias.

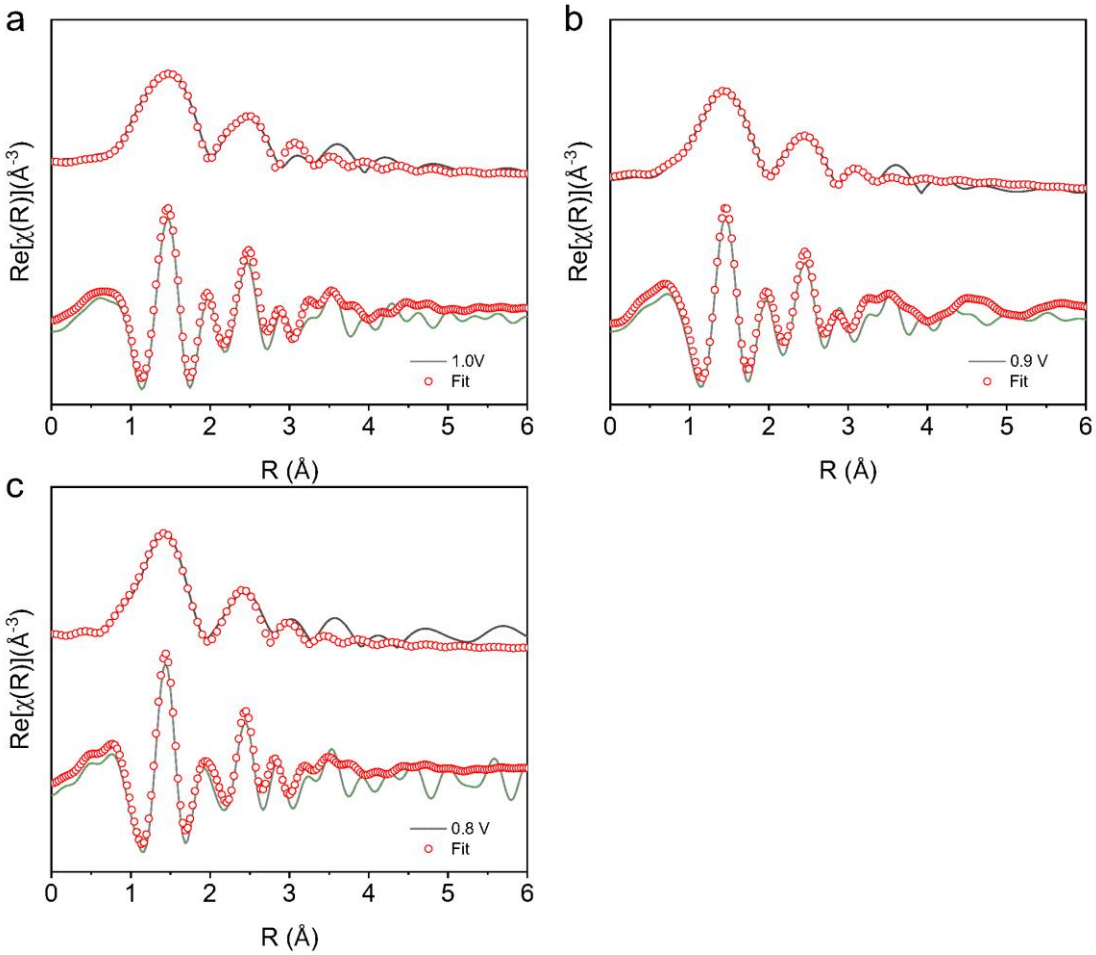

Figure S24. EXAFS fitting results of the Fe *K*-edge spectra for Onion-CrFe$_{DSA}$ at different operate potentials: (a) 1.0 V, (b) 0.9 V, (c) 0.8 V.

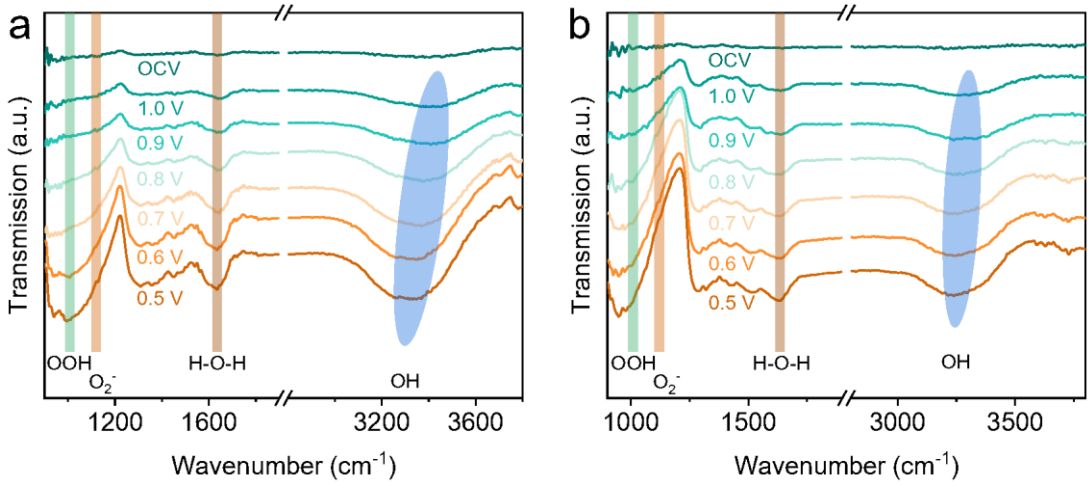

Figure S25. *Operando* ATR-SEIRAS spectra of (a) Onion-Fe_{SA} and (b) Onion-Cr_{SA} at different working potentials during ORR process.

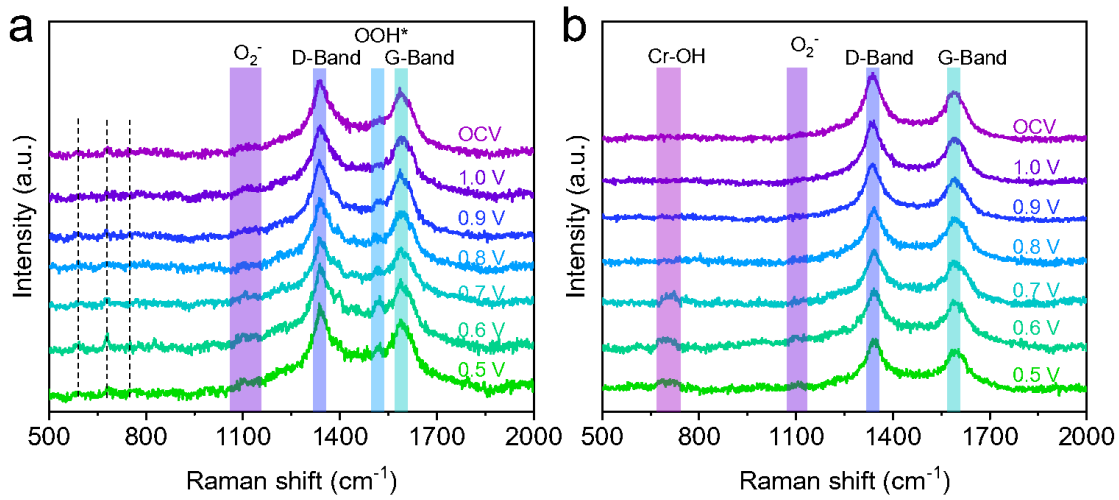

Figure S26. *Operando* Raman spectra of (a) Onion-Fe_{SA} and (b) Onion-Cr_{SA} at different working potentials during ORR process.

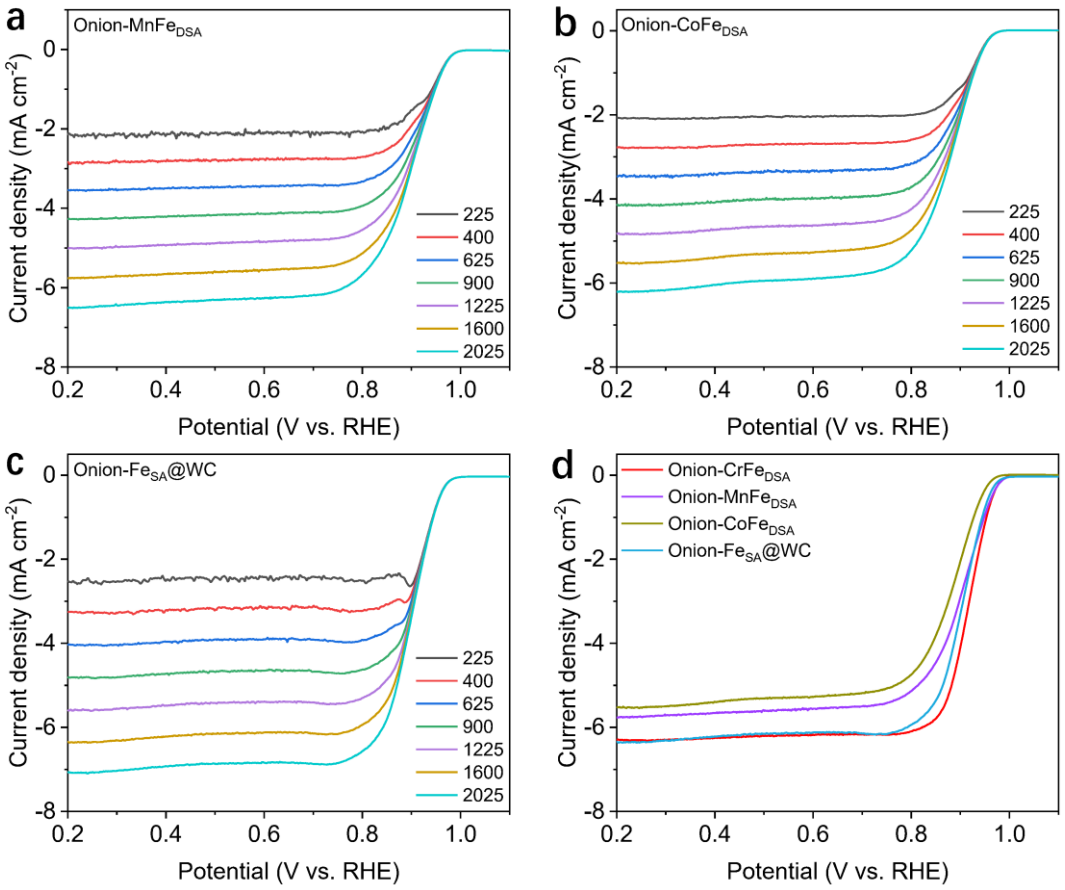

Figure S27. LSV curves of Onion-CrFe$_{DSA}$, Onion-MnFe$_{DSA}$, Onion-CoFe$_{DSA}$ and Onion-Fe$_{SA}$@WC in 0.1 M KOH electrolyte at 1600 rpm.

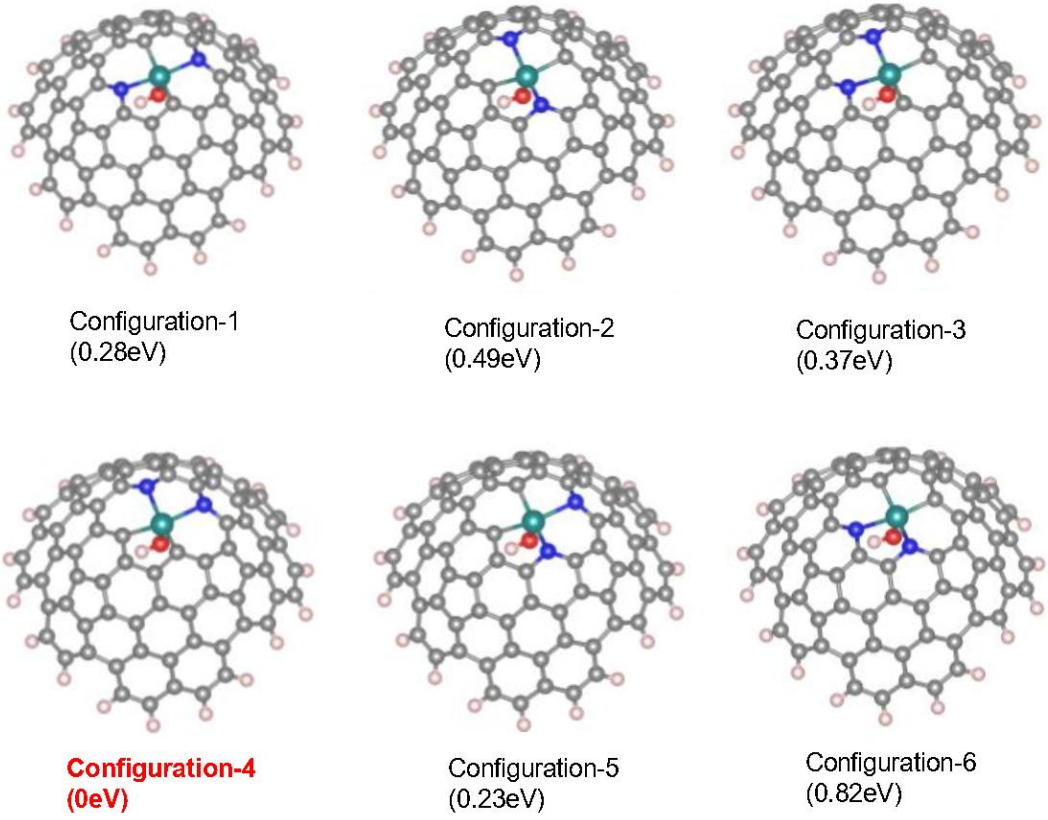

Figure S28: Schematic illustrations of various coordination structures of Onion-Cr_{SA} and their corresponding energies.

The most stable configuration (Configuration-4) was taken as the reference with its energy value set to be 0 eV, while the relative energies of other configurations were calculated with respect to this Configuration-4.

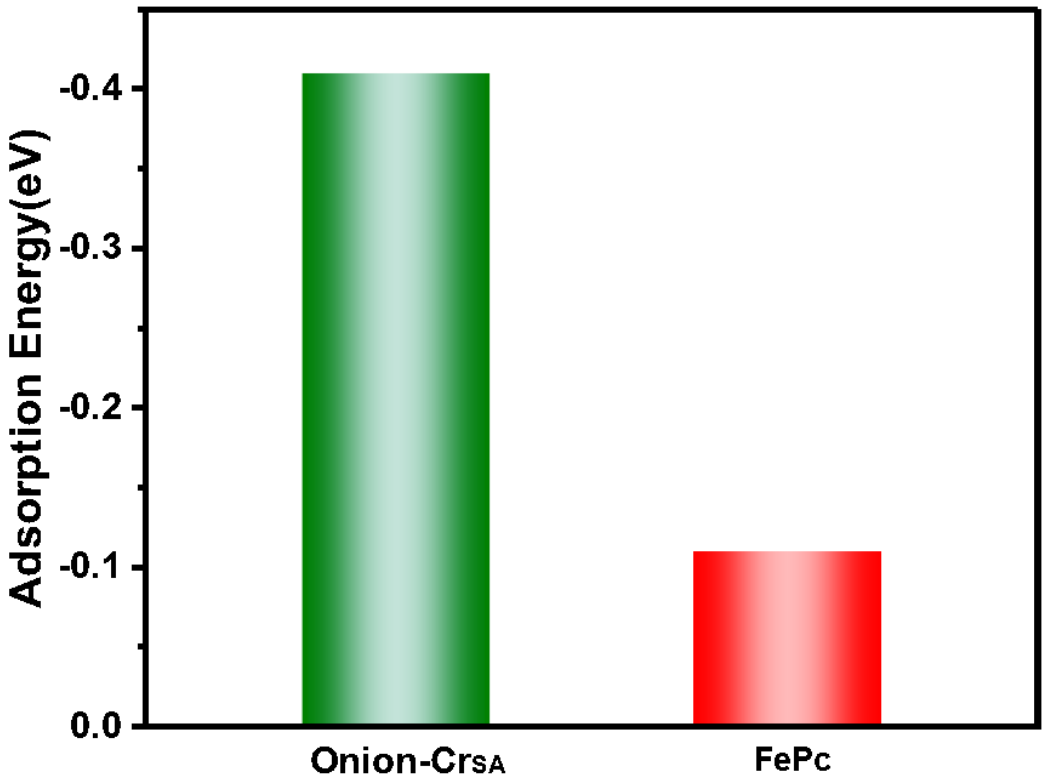

Figure S29. Adsorption energies for H_2O at FePc and Onion-Cr_{SA} surface.

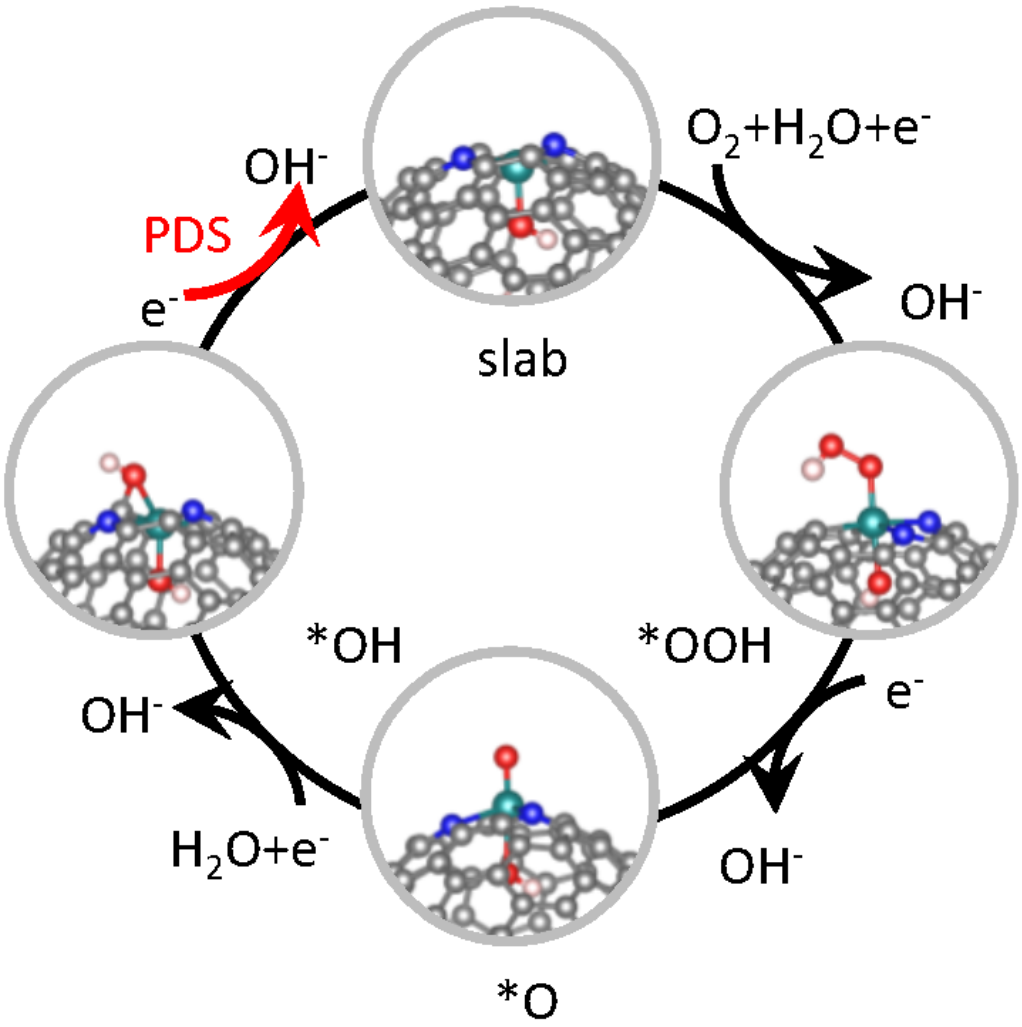

Figure S30. The reaction pathway for ORR on the Onion-Cr_{SA}

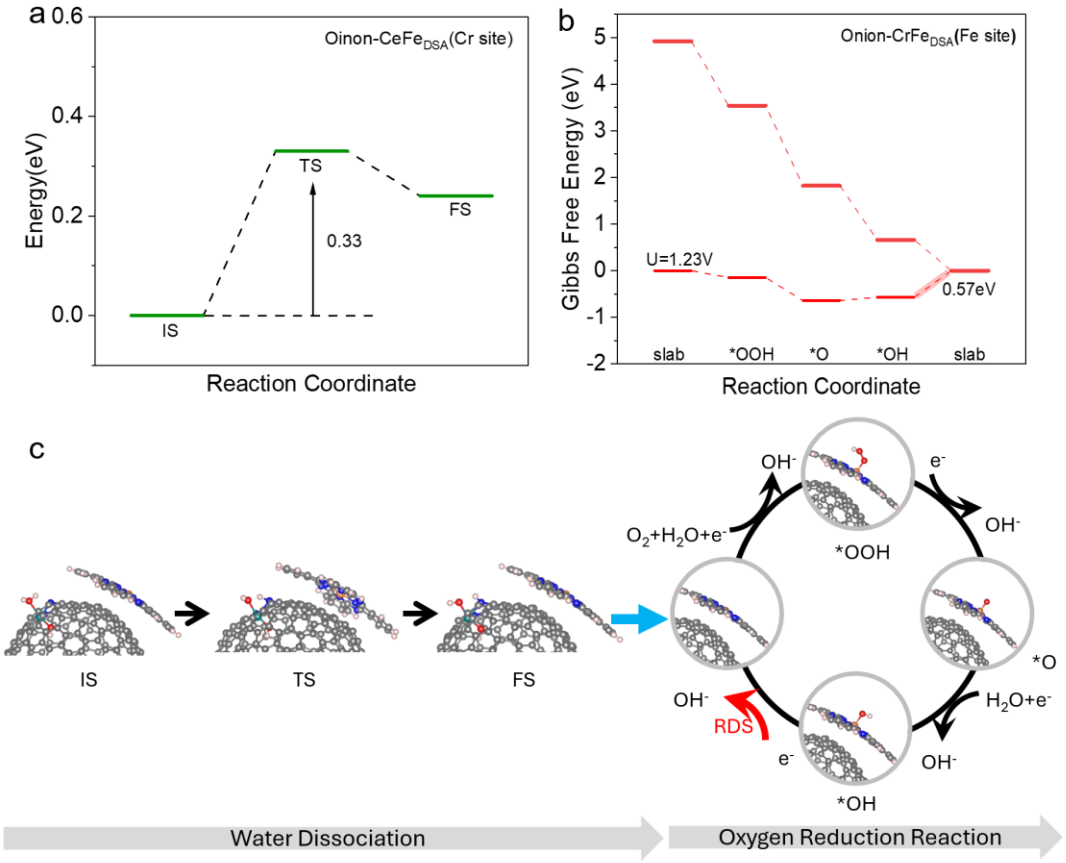

Figure S31. (a) Computed water dissociation pathway on Onion-CrFe$_{DSA}$ with Cr site. (b) Gibbs free energy diagrams for the ORR on Onion-CrFe$_{DSA}$ with Fe site. (c) Water dissociation pathway on Onion-CrFe$_{DSA}$ (Cr site) and the reaction pathway for ORR with the key intermediates on Onion-CrFe$_{DSA}$ (Fe site).

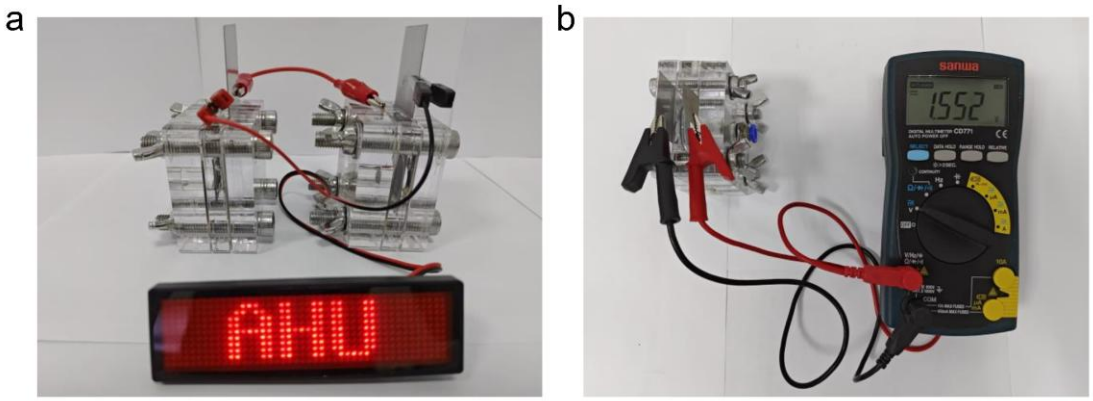

Figure S32. (a) Digital photograph of a red LED lighted by two Onion-$CrFe_{DSA}$-based Zn-air batteries connected in series. (b) Digital photograph of testing the open-circuit voltage of Onion-$CrFe_{DSA}$-based Zn-air battery with a multimeter.

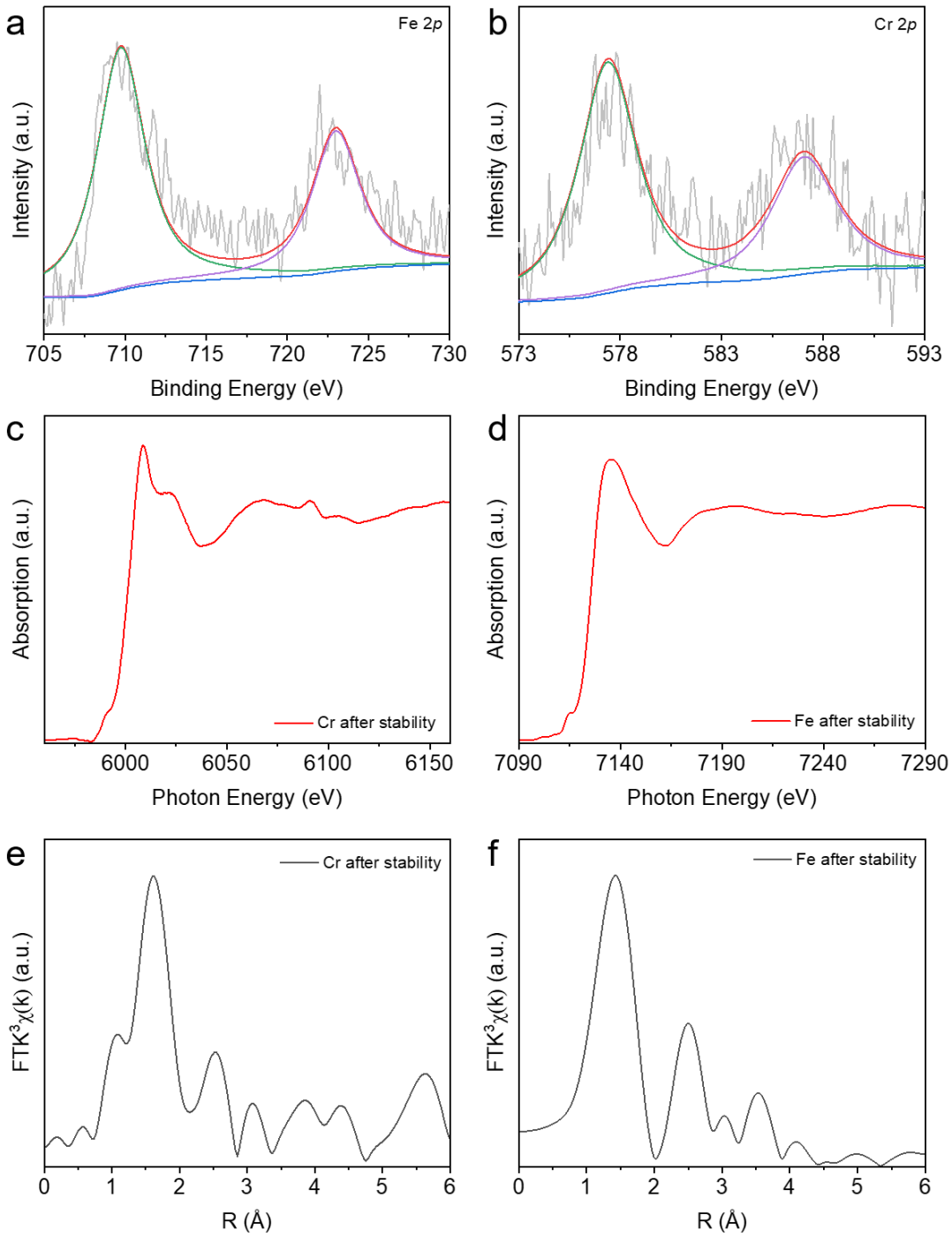

Fig. S33. (a) Fe 2*p* (b) Cr 2*p* XPS spectra of the post-cycling Onion-CrFe$_{DSA.}$ (c) Cr *K*-edge (d) Fe *K*-edge XANES spectra and the corresponding FT-EXAFS curves for (e) Cr *K*-edge and (f) Fe *K*-edge for Onion-CrFe$_{DSA}$ after atability text.

Note:

The binding energy for Fe $2p_{3/2}$ (~709.7 eV) and $2p_{1/2}$ (~723.0 eV), as well as for Cr $2p_{3/2}$ (~577.4 eV) and $2p_{1/2}$ (~587.06 eV), showed minimal deviation (all shifts <0.3 eV)

from their pre-cycling values. Furthermore, the peak shapes were well-preserved, showing no signs of significant broadening or splitting. The XANES and the corresponding FT-EXAFS spectra of Cr and Fe *K*-edge demonstrate the dual atomic structure of Cr and Fe atoms similar to the above discussions.

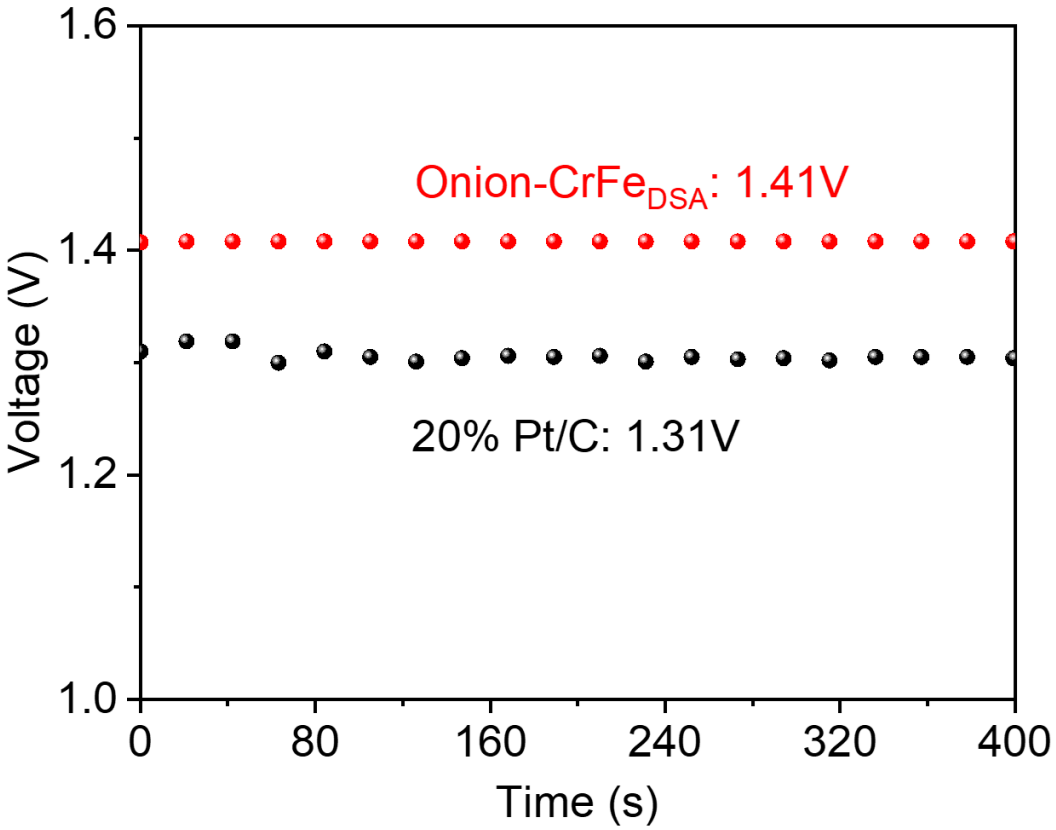

Figure S34. OCV curves of the Onion-CrFe$_{DSA}$ and 20% Pt/C assembled ZABs for 400s.

Figure S35. Flexible Quasi-Solid-State ZABs with Onion-$CrFe_{DSA}$ Catalysts Powering LEDs at Different Bending Angles (0°, 90°, 180°).

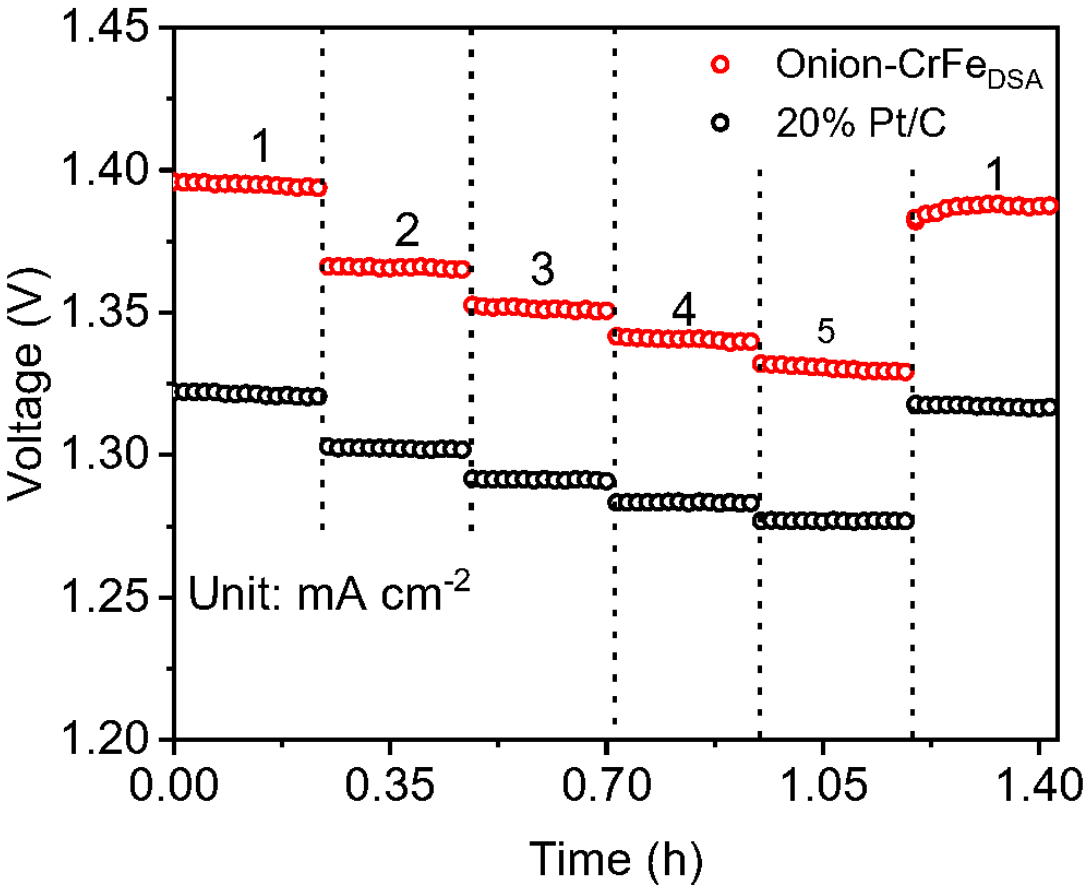

Figure S36. Discharging tests at various current densities on Onion-$CrFe_{DSA}$-based quasi-solid ZAB.

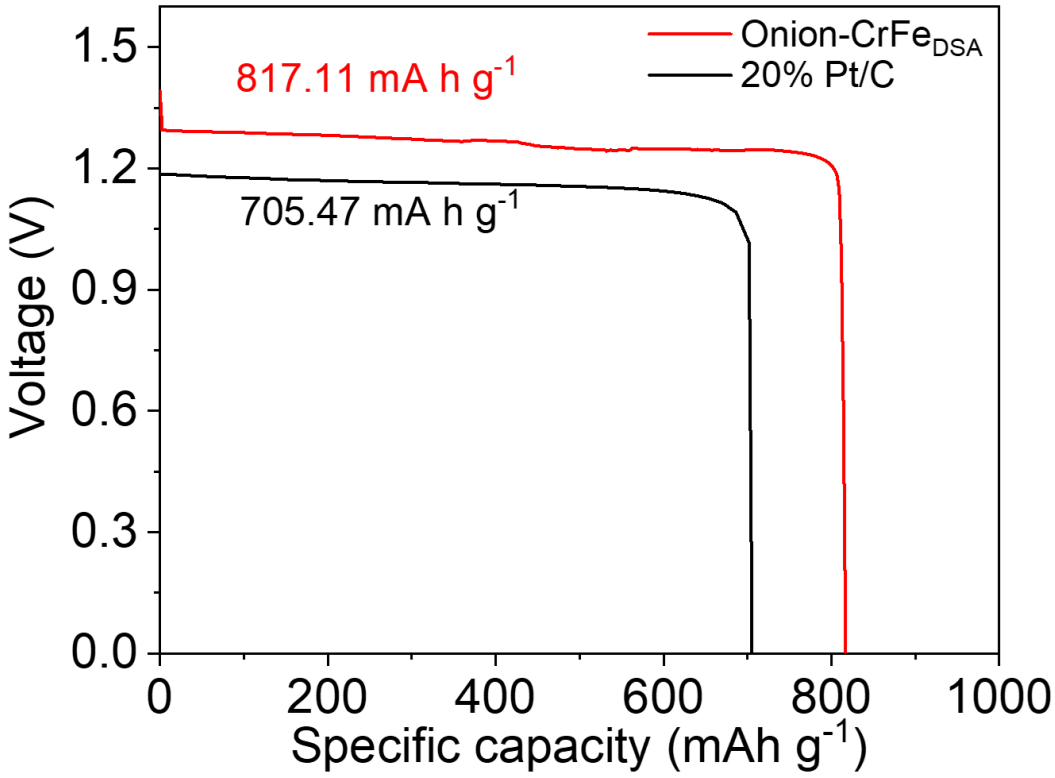

Figure S37. Specific capacity of the Onion-CrFe$_{DSA}$ based flexible ZAB compared to the 20% Pt/C.

Table S1. The metal element percentages of Onion-$CrFe_{DSA}$, Onion-Fe_{SA} and Onion-Cr_{SA} determined by ICP-AES.

Sample	Cr(wt%)	Fe(wt%)
Onion-$CrFe_{DSA}$	1.59	1.51
Onion-Fe_{SA}	-	1.55
Onion-Cr_{SA}	1.54	-

Table S2. EXAFS fitting parameters at the Cr *K*-edges.

Sample	Path	N	R(Å)	σ^2 (10^{-3} Å^2)	ΔE_0
Cr foil	Cr-Cr	8.00	2.48	5.61	3.47
	Cr-Cr	6.00	2.87	4.15	4.26
Cr_2O_3	Cr-O	3.00	1.95	1.70	-3.18
	Cr-O	3.00	2.01	1.70	-3.18
	Cr-Cr	1.00	2.65	2.60	-9.08
	Cr-Cr	3.00	2.88	2.60	-9.08
Onion-Cr_{SA}	Cr-N/C	4.05	1.99	4.03	-7.41
	Cr-C/Cr	0.51	3.01	0.02	6.46
Onion-$CrFe_{DSA}$	Cr-N/C/O	4.52	2.02	3.00	-1.37
	Cr-C/M	1.28	2.92	098	-9.19
1.0 V	Cr-N/C/O	5.43	2.01	3.95	-3.25
	Cr-C/M	1.217	2.95	1.27	-9.88
0.9 V	Cr-N/C/O	4.45	2.01	3.89	-2.59
	Cr-C/M	1.07	2.94	0.02	-9.01
0.8 V	Cr-N/C/O	5.34	2.00	4.10	-3.48
	Cr-C/M	0.78	2.95	1.5	-8.89
After bias	Cr-N/C/O	4.58	2.00	2.85	-3.53
	Cr-C/M	0.797	2.69	2.56	10.616

Table S3. EXAFS fitting parameters at the Fe *K*-edges.

Sample	Path	N	R(Å)	σ^2 (10^{-3} Å^2)	ΔE_0
Fe foil	Fe-Fe	8.00	2.46	4.89	5.57
	Fe-Fe	6.00	2.84	6.05	5.49
FePc	Fe-N	4.00	1.97	9.14	-3.18
	Fe-C	8.00	2.98	7.53	0.48
Onion-Fe_{SA}	Fe-N/O	4.23	1.99	2.91	3.20
	Fe-C	8.00	2.96	9.38	1.12
Onion-$CrFe_{DSA}$	Fe-N/O	5.15	2.00	9.14	7.30
	Fe-C/Cr	7.50	2.91	8.02	-0.16
1.0 V	Fe-N/O	6.00	1.94	9.83	8.03
	Fe-C/Cr	6.58	2.98	2.55	6.58
0.9 V	Fe-N/O	5.54	1.98	3.4	-7.77
	Fe-C/Cr	5.97	2.96	3.66	5.11
0.8 V	Fe-N/O	5.80	1.99	6.67	8.98
	Fe-C/Cr	3.86	2.91	0.34	1.82
After bias	Fe-N/O	3.91	2.01	6.33	9.86
	Fe-C/Cr	6.80	2.90	6.22	0.23